Petroleum Science 23 (2026) 2348–2366

Contents lists available at ScienceDirect

Petroleum Science

journal homepage: www.keaipublishing.com/en/journals/petroleum-science

Original Paper

The reactivation of pre-existing faults and their controlling effects on the formation of rift basin: A case from the Enping-17 Sag in the Pearl River Mouth Basin, South China Sea

Zhi-Qing Zhang [a,b], Hua Liu [a,c,1,*], Guang-Rong Peng [d], Yin Liu [a,c,1,**], Zu-Lie Long [d]

[a] National Key Laboratory of Deep Oil and Gas, China University of Petroleum (East China), Qingdao, 266580, Shandong, China
[b] School of Geosciences, China University of Petroleum (East China), Qingdao, 266580, Shandong, China
[c] Laboratory for Marine Mineral Resources, Qingdao Marine Science and Technology Center, Qingdao 266237, Shandong, China
[d] Shenzhen Branch of CNOOC Ltd., Shenzhen, 518054, Guangdong, China

ARTICLE INFO

Article history:
Received 14 May 2025
Received in revised form
24 September 2025
Accepted 7 January 2026
Available online 13 January 2026

Edited by Xi Zhang and Jie Hao

Keywords:
Rift basin
Pre-existing faults
Fault reactivation
Formation mechanisms
Pearl River Mouth Basin

ABSTRACT

The reactivation of pre-existing faults exerts a profound influence on the formation of rift basins and the deformation behaviors within their interiors, however, the specific modes of activation and underlying mechanisms remain unclear. The Enping-17 Sag, located in the tectonically active Pearl River Mouth Basin of the South China Sea, exhibits complex fault geometries and rapid subsidence since the Neogene. Its distinctive coexistence and differential reactivation of inherited fault sets make it an ideal location to investigate structural inheritance and basin evolution. In this study, high-resolution three-dimensional seismic data were employed in conjunction with seismic interpretation, dynamic analysis, and kinematic modeling to investigate the geometric attributes, activity, and genesis of sag-controlling faults. The results reveal that the boundary faults of Enping-17 Sag exhibit significant variations in strike, transitioning from a near N–S-trending in its southern segment to an ENE-trending in its northern segment. In cross-sectional profiles, the northern segment exhibits a ramp-flat geometry and records four distinct depositional periods (Early Wenchang, 49–43 Ma; Late Wenchang, 43–39 Ma; Enping, 39–32 Ma; Zhuhai, 32–23.8 Ma), whereas the southern segment displays a listric geometry, recording two prominent depositional periods (Early Wenchang, 49–43 Ma; Late Wenchang, 43–39 Ma) of tectonic reactivation. The fault displacement-length profile further indicates clear along-strike segmentation of the Enping-17 boundary fault, with variations in fault activity playing a significant role in controlling sag formation and internal structural heterogeneity. The structural evolution of the Enping-17 Sag reflects the interplay between pre-existing fault reactivation and regional tectonics along the northern South China Sea margin. Driven by Pacific Plate subduction and India–Eurasia collision, evolving extensional stresses selectively reactivated NE-trending and N–S-trending basement faults during the Early Eocene, facilitating rapid linkage of northern and southern fault segments. Continued clockwise stress-field rotation in the Middle Eocene promoted the development of new ENE-trending faults, while sustained NE-trending and ENE-trending fault activity in the Late Eocene steered the depocenter northward. Ultimately, segmented fault reactivation and progressive linkage, modulated by regional plate interactions, governed the sag's structural complexity and depositional evolution.

1. Introduction

The reactivation of pre-existing faults has been extensively observed in rift basins across the globe. Structural inheritance, spanning Precambrian and Paleozoic shear zones to Mesozoic thrust systems, has been recognized as a fundamental control on fault architecture, including fault geometries, segmentation, and creation of depocenters. Insights from seismic and geological

* Corresponding author.
** Corresponding author.
E-mail addresses: liuhua77@upc.edu.cn (H. Liu), liuyin@upc.edu.cn (Y. Liu).
Peer review under the responsibility of China University of Petroleum (Beijing).
[1] Both authors contributed equally to the supervision of this work.

https://doi.org/10.1016/j.petsci.2026.01.010

studies in diverse tectonic settings, such as the North Sea (Deng et al., 2017), North Atlantic margins (Schiffer et al., 2020), East Asia (Lou et al., 2022; Wang et al., 2022; Tang et al., 2023; Li et al., 2024), the Norwegian margin (Whipp et al., 2014), the Barents Sea (Serck and Braathen, 2019), and the Great South Basin (Phillips and McCaffrey, 2019) consistently show that fault reactivation significantly influences fault network evolution, linkage styles, and the migration of depocenters during multiphase rifting.

Previous research has been carried out on how inherited structures influence the development of rift systems, integrating methods such as seismic interpretation, structural restoration, kinematic modeling, and numerical simulation. Among these, seismic and geological data reveal fault reactivation and linkage patterns (Kim et al., 2023; Samsu et al., 2023), while modeling studies clarify the kinematic behavior of inherited structures under different stress conditions (Žalohar and Vrabec, 2010; Henza et al., 2011; Bonini et al., 2012; Gabrielsen et al., 2016; Chen et al., 2022). Field studies in the regions such as Sicily, the Southern North Sea, and Campi Flegrei further emphasize the different mechanical behaviors of inherited faults during multiphase deformation (Cultrera et al., 2015; Maunde and Alves, 2022; Natale et al., 2024). While fault systems have been extensively studied, the processes responsible for the reactivation of pre-existing faults and their evolution through multiple tectonic phases remain poorly understood. Questions persist about what conditions initiate reactivation, how faults interact under shifting stress regimes, and the extent to which these processes influence basin architecture and sedimentation. These challenges are particularly evident in fault-controlled sag basins, where irregular boundary fault geometries, asymmetric depocenters, and complex fault networks differ from classical rift patterns, highlighting the need to consider structural controls associated with multiphase extension, fault reactivation, and segmentation.

The South China Sea represents a magma-poor passive margin developed through complex lithospheric extension during the Cenozoic. Its formation involved multiple interacting geodynamic processes, including slab rollback of the paleo-Pacific Plate, retreat of the proto-South China Sea, and upwelling-induced lithospheric thinning (Briais et al., 1993; Huang et al., 2005; Hall, 2012; Pichot et al., 2014). Compared with classical Atlantic-type margins, the South China Sea exhibits asymmetric rifting, multi-directional extension, and strain localization associated with inherited Mesozoic structures (Savva et al., 2014; Huang et al., 2019; Zhao et al., 2020). Recent studies highlight that lithospheric thinning in the northern South China Sea was controlled by depth-dependent stretching and lower crustal flow, which induced strong lithospheric decoupling and non-uniform rift architecture (Bai et al., 2019; Ma et al., 2025). Despite increasing interest in margin-scale processes, how inherited structural fabrics interact with evolving stress fields during the evolution of rift segments, such as the Enping-17 Sag, remains insufficiently understood.

The Enping-17 Sag, located in the southwestern Zhu I Depression of the Pearl River Mouth Basin in the South China Sea, is a semi-graben system characterized NE-trending boundary faults with locally developed near N–S-oriented segments, and associated secondary faults (Ye et al., 2018a; Deng et al., 2021; Cai et al., 2022). Pre-existing basement faults, commonly oriented ENE–WSW or WNW–ESE due to Mesozoic tectonics (Li and Li, 2007; Shi and Li, 2012), are widely recognized as mechanically favorable planes for subsequent reactivation during Cenozoic rifting (Ye et al., 2018b, 2020; Hui et al., 2022; Ji et al., 2025). However, clear criteria for their identification remain debated. This pattern reflects the long-term interaction between reactivated Mesozoic basement structures and evolving Cenozoic extensional stress regimes (Ye et al., 2018b; Zhang et al., 2019; Deng et al., 2021; Ji et al., 2025). Although recent advances in high-resolution 3D seismic imaging have improved fault characterization (Wu et al., 2016; Cai et al., 2022; He et al., 2022), key aspects such as the kinematic evolution, fault linkage history, and their influence on stratigraphic subsidence and generation of depocenters remain unclear. Therefore, this study focuses on reconstructing the reactivation history of boundary faults in the Enping-17 Sag using integrated 3D seismic interpretation, structural and stratigraphic analysis, and physical modeling. By examining how pre-existing NE–SW and N–S basement faults were reactivated during multiphase extension, and how they subsequently contributed to the nucleation and linkage of new fault segments, this study aims to clarify their influence on fault geometry, segmentation patterns, subsidence evolution, and the formation of syn-rift depocenters in this atypical rift basin.

2. Geological setting

2.1. Tectonic framework

The Pearl River Mouth Basin (PRMB) is located in the middle of the northern continental margin of the South China Sea, and represents the largest Cenozoic rift basin in the region (Fig. 1). It trends overall NE–SW, parallel to the main continental margin, and is subdivided into five compartments inside the basin arranged in a NE-striking orientation: Northern Uplift Belt, Northern Depression, Central Uplift Belt, Southern Depression, and Southern Uplift Belt (Shi et al., 2009; Yin, 2010; Liu et al., 2021). Among these, the Zhu I Depression occupies the eastern part of the Northern Depression Belt, which contains the Enping Sag, Xijiang Sag, Huizhou Sag, Lufeng Sag, and Hanjiang Sag (Fig. 1(a)). The depression exhibits a structural pattern characterized by north–south subdivision into distinct structural zones and east–west segmentation into separate compartments (Cao et al., 2014; Li et al., 2023).

The Enping-17 Sag is situated within the Enping Depression in the northwestern part of the PRMB, with an overall NE–SW orientation and an area of about ca. 5000 km^2. It is bounded to the east by the Enping-12 Sag and Enping-18 Sag, and to the north and south by the Northern Uplift Belt and Panyu Low Uplift, respectively (Fig. 1(b)). Structurally, the Enping-17 Sag and Enping-12 Sag are controlled by NE-trending boundary faults that locally display N–S-oriented segments in the northwestern part of the depression, while the Enping-18 Sag is bounded by an E–W-trending fault along the northern margin.

Regionally, the PRMB hosts a complex system of pre-existing faults and has experienced multiple tectonic phases (Ye et al., 2018b, 2020; Peng et al., 2022). During the Early Upper Cretaceous (100 Ma), the subduction of the paleo-Pacific Plate induced a compressional stress regime, resulting in the development of WNW–ESE-trending to E–W-trending thrust faults (Shi and Li, 2012; Zhu et al., 2015). This transitioned into a back-arc extensional setting in the Late Cretaceous (100–66 Ma), generating NE–SW and ENE–WSW normal faults that later guided Cenozoic rifting (Morley, 2012, 2016). Since the Cenozoic, the basin underwent three major extensional phases: Rift Ia (Zhuqiong I Movement, 49–43 Ma) was dominated by NW–SE extension, which reactivated ENE–WSW-trending and WNW–ESE-trending basement faults and initiated NE–SW-striking normal faults that contributed to the formation of early half-graben structures. This extensional phase is widely attributed to the rollback of the subducting paleo-Pacific Plate, which induced trench retreat and back-arc stretching along the northern South China Sea margin (Morley, 2002; Li and Li, 2007). Rift Ib (Huizhou Movement, 43–39 Ma) marked a clockwise rotation of the regional stress field to an

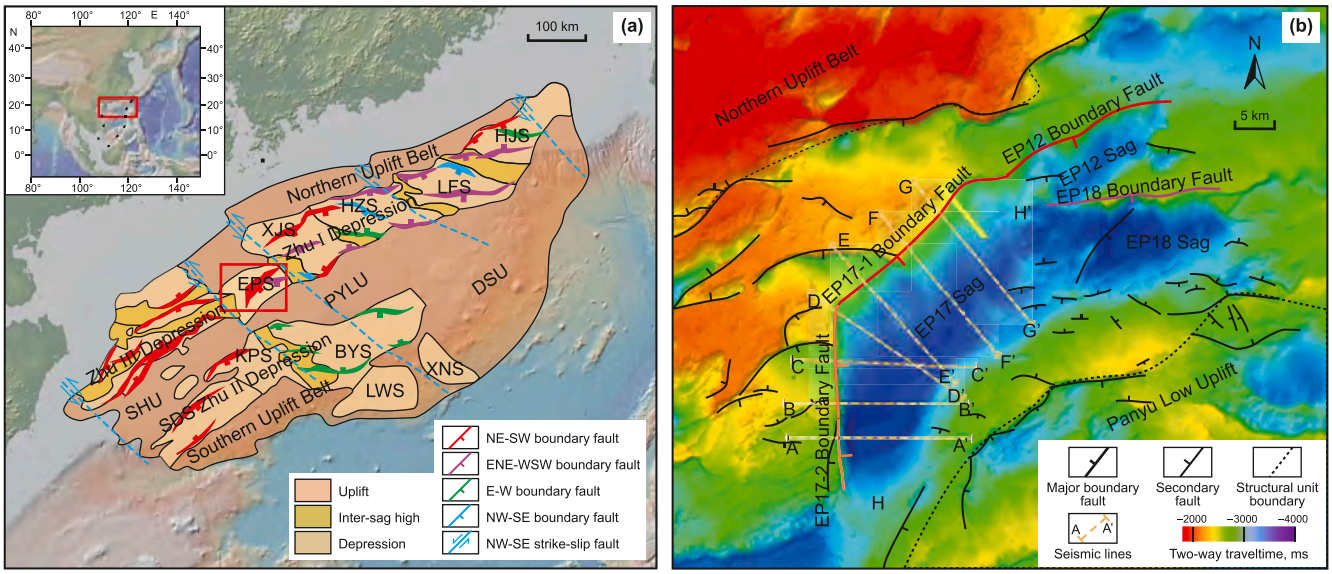

Fig. 1. Regional tectonic setting and fault distribution of the Enping-17 Sag. **(a)** Tectonic setting and structural framework of the PRMB, with the red rectangle marking the Enping-17 Sag. The inset shows the PRMB in the northern South China Sea. Simplified fault traces are interpreted from 3D seismic data and previous studies (Ye et al., 2018b; Deng et al., 2021; Hui et al., 2022; Ji et al., 2025). **(b)** Major faults and tectonic units of the Enping-17 Sag. Colored lines denote boundary faults interpreted as basement-involved extensional structures; thin black lines show secondary faults, black dotted lines indicate uplift–sag boundaries, and yellow dotted lines mark seismic profile locations. (HJS: Hanjiang Sag; LFS: Lufeng Sag; HZS: Huizhou Sag; XJS: Xijiang Sag; EPS: Enping Sag; KPS: Kaiping Sag; BYS: Baiyun Sag; LWS: Liwan Sag; XNS: Xingning Sag; PYLU: Panyu Low Uplift; DSU: Dongsha Uplift; SHU: Shenhu Uplift. These names represent first-order structural units.)

NNW–SSE orientation. This change enhanced activity along NE-striking faults, promoted segmentation and linkage of major boundary faults, and increased structural complexity within the sags. It is interpreted as the combined effect of far-field compressional stresses from the India–Eurasia collision and contemporaneous changes in paleo-Pacific subduction dynamics, which modified the extensional regime along the South China margin (Shi et al., 2020; Hao et al., 2021). Rift II (Zhuqiong II Movement, 39–32 Ma) was characterized by near N–S extension, which facilitated the development of E–W-trending faults and oblique deformation, accompanied by a northwestward migration of depocenters. This stage corresponds to the incipient opening of the South China Sea, driven by slab rollback and seafloor spreading in the East Sub-basin, which imposed a nearly N–S extensional regime across the northern margin (Wu et al., 2016; Ye et al., 2018b; Tang et al., 2023). During the post-rift stage, NE-directed extension has been interpreted to promote localized transtension and strike-slip faulting, particularly in southwestern sags such as the Yangjiang Sag, where NW-trending pull-apart structures have been documented (Shu et al., 2008; Hu, 2019; Li et al., 2019; Duan et al., 2020; Hui et al., 2021; Wang et al., 2021).

In contrast, previous studies have described deformation in the Enping-17 Sag as predominantly accommodated by multiphase extensional faulting throughout the Cenozoic (Ye et al., 2018a; Deng et al., 2021; Cai et al., 2022). The main NE-trending boundary faults are reported to record normal displacement during the syn-rift stages. While regional investigations have documented strike-slip reactivation and transtensional deformation in parts of the southwestern PRMB (Hu, 2019; Ma et al., 2021; Hui et al., 2022; Ji et al., 2025), published interpretations of the Enping-17 Sag have focused on extensional structures (Ye et al., 2018a; Zhang et al., 2019; Deng et al., 2021).

2.2. Stratigraphic framework

The Cenozoic tectonic evolution of the region can be subdivided into two major stages: syn-rift and post-rift (Fig. 2). The syn-rift stage experienced three tectonic phases: Zhuqiong I Movement, Huizhou Movement, and Zhuqiong II Movement, which collectively resulted in the development of key regional unconformities at seismic horizons Tg, T83, and T80 (Wang et al., 2015; Wu et al., 2016; Ye et al., 2018b). During this stage, the Wenchang and Enping formations were deposited in lacustrine and deltaic environments, with the Wenchang Formation stratigraphically subdivided by the T83 seismic horizon into lower and upper sections (Shi et al., 2020). Specifically, the Upper Wenchang Formation (above horizon T83) comprises three third-order sequences, informally referred to as the first, second, and third intervals of the Upper Wenchang Formation (WC1, WC2, and WC3), corresponding to horizons T80, T81, and T82. The Lower Wenchang Formation (below horizon T83) comprises three third-order sequences, informally referred to as the first, second, and third intervals of the Lower Wenchang Formation (WC4, WC5, and WC6), corresponding to horizons T83, T84, and T85 (Fig. 2). Lithologically, the Wenchang Formation mainly consists of thick-bedded mudstone layers with interbedded thin sandstone layers, whereas the Enping Formation shows an inverse pattern, featuring extensive sandstone development intercalated with thin-bedded mudstone (Ge et al., 2020). The post-rift stage is represented by five major formations: the Paleogene Zhuhai Formation and the Neogene Zhujiang, Hanjiang, Yuehai, and Wanshan formations (Fig. 2). The Zhuhai Formation is characterized by thick-bedded sandstone, while the Neogene strata are dominated by extensively deposited thick mudstone in shallow sea environments (Xiong et al., 2020; He et al., 2022; Zhu et al., 2022).

3. Data and methods

3.1. Data

This study used newly acquired (2023) pre-stack time-migrated high-resolution 3D reflection seismic data, processed and provided by the China National Offshore Oil Corporation (CNOOC) Shenzhen Branch. The Enping-17 Sag, covering an area of ca. 400 km^2, specifically focuses on the rift-stage sag-controlling

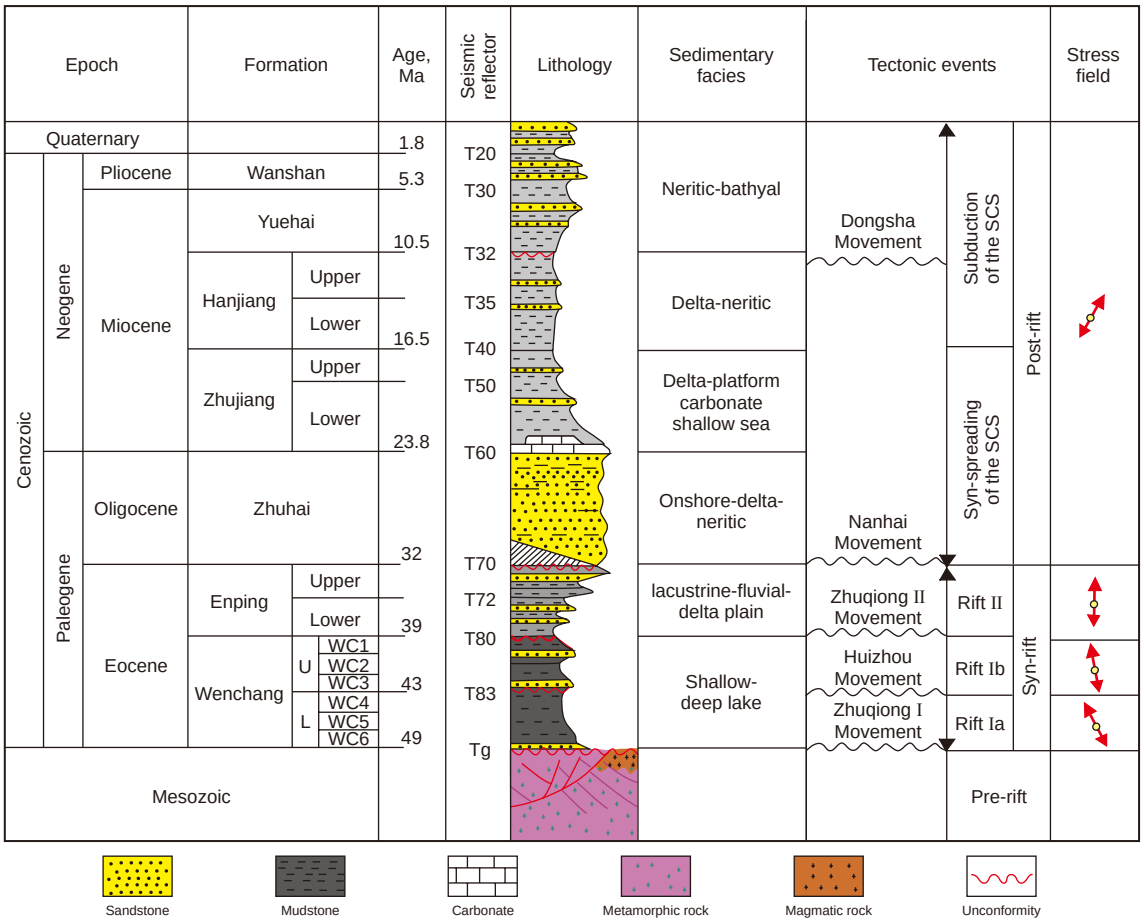

Fig. 2. Composite stratigraphic column of the Pearl River Mouth Basin and its regional tectonic events (modified from Ge et al., 2020).

boundary faults. The 3D seismic dataset has a bin spacing of 12.5 m in both inline and crossline directions. It was acquired with a sampling interval of 2 ms and an average dominant frequency of 30 Hz, which gives a vertical resolution of ca. 20 m. All seismic sections in this study are displayed in two-way travel time (TWT). The interpreted seismic horizons spans from ca. 2000 ms at the top of the Paleogene strata (T70) down to ca. 5000 ms at the Mesozoic basement (Tg), including eleven key horizons (Tg, T85, T84, T83, T82, T81, T80, T73, T72, T71, T70). These interpreted horizons are well constrained by ca. 60 wells, covering most parts of the study area, although only a few penetrate the Paleogene strata. We conducted detailed seismic interpretations along the Enping-17 boundary fault, covering ca. 4.5 km in length with 10 m interpretation intervals. We analyzed thousands of seismic lines, oriented from E–W to NW, to clarify the fault's geometry. All seismic interpretations used to define fault geometries and horizon offsets were performed manually in Petrel software, following established structural interpretation criteria.

Additionally, time-depth conversion was performed by using a fitted linear polynomial based on well checkshot data, $D = 1.9131T - 1143.3$ ($R^2 = 0.9836$). Due to velocity heterogeneity and data scatter, a linear approximation was adopted despite the moderate correlation (Fig. 3).

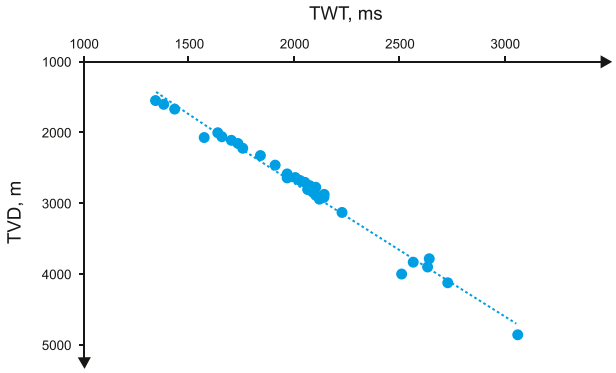

Fig. 3. Time-depth conversion for seismic mapping was based on 24 wells in the study area. The fitted linear function is $D = 1.9131\ T - 1143.3$ (D: true vertical depth in m; T: two-way travel time in ms).

3.2. Methods

3.2.1. Seismic-based methods

Based on seismic data and structural interpretation, this study employs a combination of techniques to assess fault reactivation and evolution, including throw-distance (T–x) plots, throw-depth (T–z) plots, fault expansion index (EI) values, and fault activity rates. Here, fault activity is assessed through variations in throw magnitude and stratigraphic thickening, providing quantitative insight into reactivation timing and intensity along the boundary faults. Fault throw was calculated as the vertical stratigraphic separation between correlative horizons across the fault surface. Previous studies have shown that the distribution patterns of fault throw variations in T–x and T–z plots are generally similar in the time and depth domains (Tvedt et al., 2013; Ryan et al., 2017). Therefore, throw values are measured in meters in this study.

T–x plots are constructed by extracting throw values along the interpreted fault trace at each stratigraphic horizon and plotting them against along-strike distance. On *T–x* plots, maximum throws indicate fault nucleation points, whereas minimum throws between adjacent maxima typically represent fault linkage zones (Kim and Sanderson, 2005; Giba et al., 2012; Maunde and Alves, 2022). In this study, the sampling interval for the *T–x* plot is set to 0.2%–0.5% of the total fault length to ensure capture of localized variations, providing 1232 evenly distributed data points along the fault.

T–z plots are generated by plotting fault throw values for multiple horizons against depth, allowing reconstruction of vertical displacement accumulation and insights into fault propagation history. Gentler slopes on the *T–z* plot indicate a more rapid reduction in throw with decreasing depth, representing stronger fault activity. In contrast, a near-vertical *T–z* trend suggests minimal variation in throw, representing a period of fault inactivity (Peacock and Sanderson, 1991; Baudon and Cartwright, 2008; Jackson and Rotevatn, 2013; Maunde et al., 2021). Additionally, the geometry of *T–z* plots can distinguish isolated, growth, dip-linked, and reactivated faults (Peacock, 2002).

Expansion index (EI) is also used to evaluate the differential thickening of growth strata across faults, and is defined as the ratio of hanging wall to footwall stratigraphic thickness within the same interval (Eq. (1)).

$$\mathrm{EI} = \frac{H_{\mathrm{hw}}}{H_{\mathrm{fw}}} \tag{1}$$

where H_{hw} and H_{fw} are the thicknesses (in time or depth) of a given stratigraphic unit in the hanging wall and footwall, respectively. An EI greater than 1 indicates significant syn-depositional fault activity, with greater values implying stronger activity (Thorsen, 1963; Gawthorpe and Leeder, 2000). In this study, EI values are not quantitatively analyzed but are instead used as qualitative indicators of fault activity intensity. This approach focuses on the vertical component of displacement and assumes that growth strata geometry during the syn-rift stage is primarily controlled by dip-slip motion. Although minor strike-slip or transtensional features are visible in strata above the T70 horizon, these are interpreted as later overprints and are unlikely to have significantly influenced the syn-depositional displacement. The impact on EI estimation is therefore considered limited.

In this study, fault activity is used as a proxy to describe fault reactivation and evolutionary intensity. It is defined as the relative degree of displacement, characterized by throw-depth (*T–z*) and expansion index (EI) values, rather than absolute slip rates. This approach provides a workable measure of activity in rift settings where precise age constraints are lacking, and has been widely adopted in similar tectonic studies.

3.2.2. Physical model experimental set-up

In this study, a sandbox model (Withjack and Jamison, 1986; Tron and Brun, 1991; Bonini et al., 1997; Keep and McClay, 1997; Dooley and Schreurs, 2012; Tong, 2012) was used to simulate the syn-rift deformation of Enping-17 Sag boundary faults. The experimental area is rectangular measuring 36 cm in length and 24 cm in width (Fig. 4). The physical modeling aims to explore how obliquely oriented, predefined traces in the PDMS basement accommodate NW–SE-directed extension. Particular attention is given to the sequence of deformation, the potential for geometric linkage, and their spatial association with developing surface structures. These traces follow orientations inferred from seismic interpretation and act as geometric constraints that guide deformation under controlled laboratory conditions. The model base is a

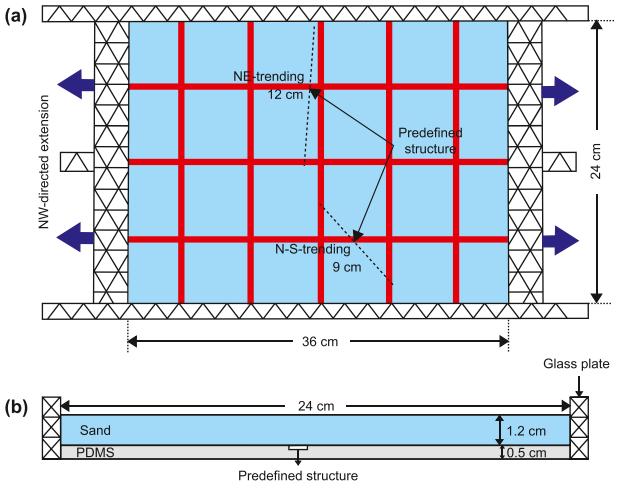

Fig. 4. Schematic setup showing the predefined structures in the PDMS layer. **(a)** Plan view. **(b)** Cross-sectional view. Arrows indicate the imposed NW–SE extensional direction. PDMS: polydimethylsiloxane, simulating the ductile basement.

24 cm wide glass plate covered with 0.5 cm thick layer of polydimethylsiloxane (PDMS) to represent a ductile basement. The PDMS has a density of 0.965 g/cm^3 and a viscosity of ca. 10^4 Pa s (Weijermars, 1986; Withjack and Jamison, 1986; Henza et al., 2010; Tong et al., 2014). Thin wooden rods were used to gently score shallow grooves (1–2 mm deep) into the PDMS surface, defining the initial fracture positions as mechanical discontinuities: a 12 cm NE-trending groove in the northern part of the model and a 9 cm N–S-trending groove in the south. These weak zones localized strain during extension without constraining the initial dip angle. The scale of the faults is referenced to the actual dimensions of the Enping-17 boundary faults, in which 1 cm in the model represents 1 km in reality.

Loose blue quartz sand was used to simulate the brittle layer in the sandbox model. The grain size of the blue quartz sand ranges from 160 μm to 300 μm, and its mechanical behavior conforms to the Coulomb failure criterion. Dry quartz sand has negligible cohesion (30 Pa) and an internal friction angle of approximately 31° (Dubois et al., 2002; Lohrmann et al., 2003; Bellahsen and Daniel, 2005). To simulate the sedimentary sequence, a 1.2 cm thick quartz sand layer was applied to the model and smoothed to ensure uniformity. This process does not significantly alter the frictional properties of the granular material (Gomes and Caldeira, 2011; Gomes, 2013; Klinkmüller et al., 2016; Almqvist and Koyi, 2018) (Table 1). Additionally, to visualize the observation of fault-related displacement and layer offsets, <1 mm thick colored sand horizons were periodically embedded at 7.5 cm intervals within the quartz sand sequence (Del Ventisette et al., 2019).

The model was equipped with movable 24 cm side-length rigid steel plates on both sides (Fig. 4). To ensure deformation remained within the mechanical limits of the PDMS basement, the side plates were driven at a constant rate of 0.02 mm/s. The imposed NW–SE extension induced deformation in the overlying quartz sand, with strain preferentially localizing along the predefined structures, leading to the formation of surface structure zones. The experiment was terminated when the cumulative displacement at each boundary reached 40 mm, equivalent to 18.2% bulk extension. The total experiment duration was 2000 s.

The kinematic evolution of the model was continuously recorded by high-resolution video imaging, enabling frame-by-frame analysis of surface fracture development, displacement patterns, and progressive separation of colored marker layers.

Table 1
Physical properties of sandbox materials (adapted from Withjack and Jamison, 1986; Klinkmüller et al., 2016; Del Ventisette et al., 2019).

Sandbox materials	Grain size, μm	Bulk density, g/cm^3	Internal friction angle, °	Cohesion, Pa	Young's modulus, Pa	Poisson's ratio	Viscosity, Pa·s
Blue quartz sand	160–300	1.5–1.6	31	30	/	0.3	/
Red quartz sand	425–625	1.5–1.6	34	30	/	0.3	/
PDMS (poly-dimethylsiloxane)	/	0.965	/	/	1×10^6	0.48–0.5	3×10^4

Kinematic features include marker displacement across fracture traces, with predominantly dip-slip offsets and no significant lateral shifts. The oblique orientation of the N–S-trending fracture relative to the extension direction is geometrically consistent with localized transtensional strain.

The applied NW–SE extension was orthogonal to the NE–SW-trending trace and oblique (45°) to the N–S-trending trace. This extension direction was selected to represent the dominant stress orientation during the early syn-rift stage (Zhuqiong I Movement), as documented in previous regional studies (Zhang et al., 2019; Ji et al., 2025). While the stress orientations may have varied during later rifting phases, the experiment employed a fixed NW–SE-directed extension to ensure consistent boundary conditions and controlled observation of deformation along oblique predefined traces. The model parameters included predefined fracture strikes (NE–SW and N–S), a quartz sand internal friction angle of 31°, PDMS viscosity of 10^4 Pa·s, fault lengths of 9 cm and 12 cm, and an imposed extension rate of 0.02 mm/s.

4. Results

4.1. Structural characteristics of pre-existing and boundary faults

4.1.1. Seismic identification of pre-existing faults

The basement in the Enping-17 Sag is poorly imaged due to scattering and a low signal-to-noise ratio. Nevertheless, Fig. 5 illustrates four representative seismic expressions. In Fig. 5(a), discontinuity cuts the Tg horizon, where reflector terminations and localized offsets are visible. This feature is traceable across adjacent profiles with consistent strike-dip geometry, and is interpreted as candidate pre-existing faults. By contrast, Fig. 5(b)–(d) illustrate features regarded as non-structural

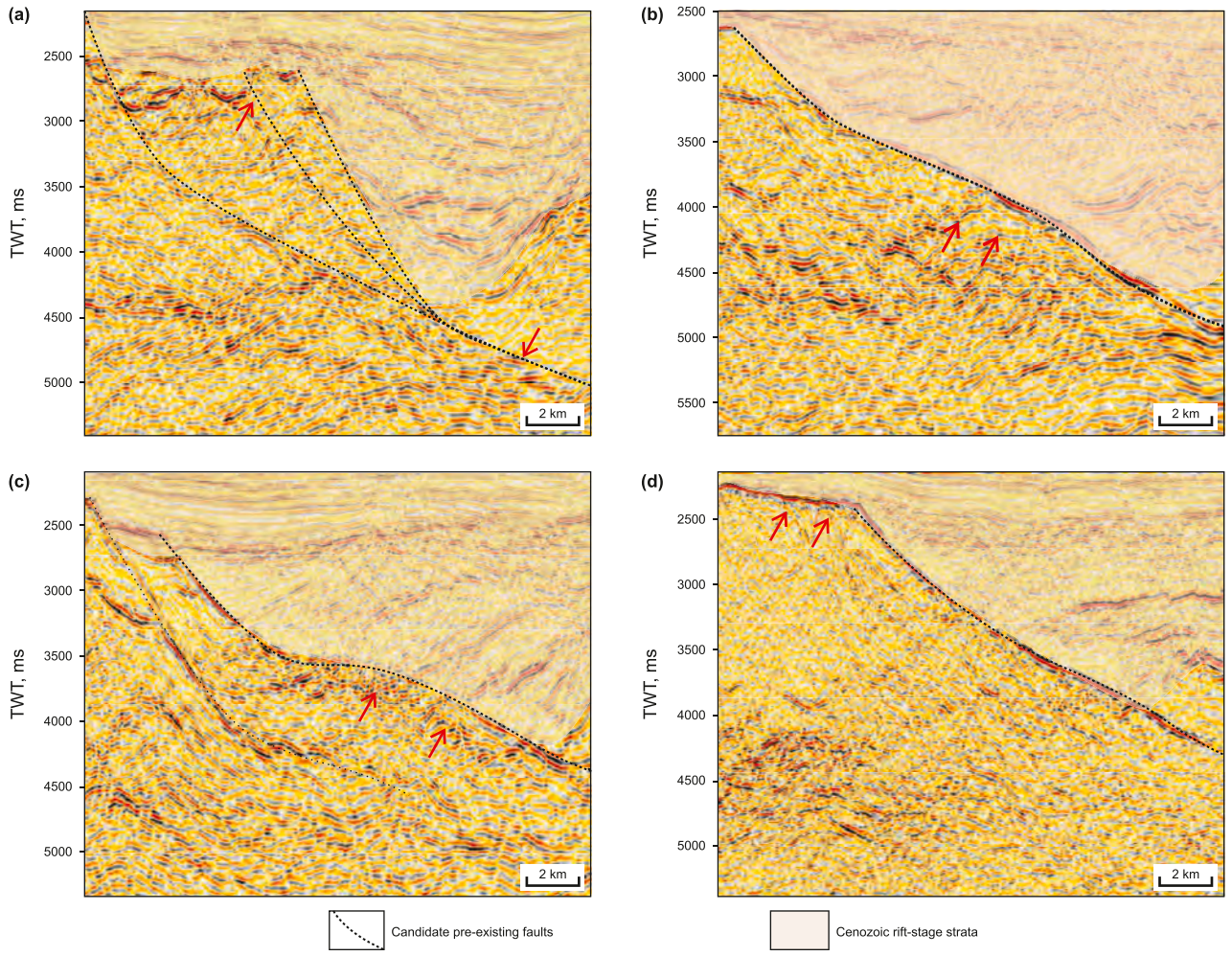

Fig. 5. Representative seismic expressions of basement-related features in the Enping-17 Sag. **(a)** A discontinuity cutting the Tg horizon with reflector terminations and localized offsets (red arrows), taken as a candidate pre-existing fault. **(b)** Multiples. **(c)** Comb-like disturbances. **(d)** Weak reflections (red arrows). Candidate faults are distinguished from artifacts based on continuity, geometry, and stratigraphic response.

artifacts and excluded from fault interpretation: periodic, sub-parallel bands typical of multiples; short, densely spaced comb-like segments with poor lateral continuity; and weak, low-amplitude reflections lacking stratigraphic response.

In this study, candidate pre-existing faults are defined as coherent reflector zones at the Tg horizon. Such features are identified where reflectors display kilometer-scale terminations or offsets, maintain consistent strike-dip geometry across adjacent profiles, and show stratigraphic coupling with Cenozoic rift-stage deposits. Some discontinuities remain confined to the Tg horizon without producing observable displacement in younger strata, whereas others extend upward and deform the syn-rift succession.

In addition to these core criteria, diagnostic fault geometries such as steep-flat-steep (S-shaped) or listric profiles are used to distinguish laterally coherent reflector zones from short, comb-like disturbances. Regional orientation is also considered: reflector zones that strike ENE or nearly N–S are noted as differing from the NW–SE syn-rift extension. Broad, kilometer-scale reflector zones are taken as mechanically more significant than thin, discontinuous reflections with limited structural plausibility. Together, these features serve as practical criteria for distinguishing basement fabrics from multiples or artifacts.

Although seismic resolution prevents direct derivation of quantitative activity parameters such as EI values, reflector geometry and stratigraphic relationships indicate consistency with basement fabrics previously recognized in the northern South China Sea (Ye et al., 2018b; Deng et al., 2021; Ji et al., 2025).

4.1.2. Geometric characterization of boundary faults

The sag-controlling boundary fault of the Enping-17 Sag extends ca. 46.4 km, displaying a generally curved geometry. The Enping-17 boundary fault system comprises two main segments, referred to here as F1 and F2. Although these segments were labeled separately to describe variations in strike and displacement, they are interpreted in 3D seismic data as geometrically connected components of a composite fault zone (see Section 4.2.2 for details and Fig. 12). Accordingly, no discrete merging occurs between independent faults; rather, the segments maintain lateral continuity while exhibiting internal segmentation.

The northern boundary fault trends NE and is designated as F1, while the southern boundary fault trends nearly N–S and is named F2 (Fig. 6(a)). In plan view, the mapped segments define a composite boundary structure. As shown in Fig. 6, interpreted boundary and secondary fault traces across multiple stratigraphic horizons illustrate gradual variations in connectivity and geometry. At the pre-Cenozoic basement (Tg), the F1–F2 system appears as a fully connected, continuous fault trace (Fig. 6(a)). Notably, the northeastern end of F1 appears geometrically linked with the EP18 boundary fault, while the linkage become less evident at shallower levels. At the top of WC6 (T85), the boundary faults are relatively short and linear (Fig. 6(b)). At the top of WC4 (T83), partial linkage is observed along F1–F2, the northeastern tip of the F1 fault deflected to an ENE orientation (Fig. 6(c)). At the top of WC1 (T80), numerous E–W-trending and ENE-trending secondary faults developed, particularly in the central and eastern sag, forming a more complex and segmented fault network (Fig. 6(d) and (e)).

These observations indicate that the F1–F2 system shows greater continuity and stratigraphic influence in the Wenchang Formation. Accordingly, F1–F2 is here defined as the composite boundary fault of the Enping-17 Sag. Structural connections with adjacent fault systems (Enping-12 and Enping-18) remain unresolved and are beyond the present scope.

Seismic profiles at different locations reveal significant geometric variations along the fault between the southern and northern sag. Fault F1 exhibits a steep-flat-steep geometry, forming an overall S-shaped profile (Fig. 7(c) and (d)). In the seismic section, it is characterized by a low-dip, sub-horizontal segment at mid-depth, flanked by steeper portions at shallower and deeper levels. The fault extends continuously across multiple stratigraphic intervals. Four rollover anticlines are observed in the F1 hanging wall. The early and late Wenchang-stage anticlines (horizons Tg–T83 and T83–T80, respectively) are clearly fault-controlled, whereas those formed during the Enping (horizons T80–T70) and Zhuhai (horizons T70–T60) stages progressively developed farther from the boundary fault.

In contrast, Fault F2 displays a listric geometry, with an initial dip of approximately 50°, and is overall steeper than F1 (Fig. 7(a) and (b)). In the seismic section, F2 is adjacent to a steep westward fault, with the two structures in contact at depth, although their spatial linkage remains unclear in map view. This adjacent fault extends into the pre-Cenozoic basement, with no observable offset in the overlying strata, and is further illustrated in the 3D structural model (see Fig. 12). Two rollover anticlines developed along the F2 hanging wall are associated with the early and late Wenchang stages. Additionally, at the basement horizon (Tg), intracrustal reflectors exhibit a broad fold geometry.

Furthermore, transverse fold is observed along the strike of the sag-controlling boundary fault during the early Wenchang stage, recorded within WC5 (T84–T85) (Fig. 8). The fold is associated with subtle but persistent structural highs oriented perpendicular to the fault trace. These features coincide with local reductions in fault continuity and may mark geometrical segment boundaries.

4.2. Fault activity and evolution

Vertical variations in fault throw were examined using *T*–*z* plots and EI values derived from seven representative seismic profiles across the Enping-17 boundary fault (Fig. 9). These profiles cover areas with contrasting fault geometries and displacement patterns. In addition, based on 3D seismic interpretation *T*–*x* plots were constructed to illustrate along-strike variations in fault throw and segmentation. All interpreted seismic horizons are labeled using T markers (T80–T85), corresponding to the tops of WC1–WC6 intervals, respectively.

4.2.1. Fault activity variations across tectonic phases

In the WC6–WC4 interval (blue-shaded), Fig. 10(a)–(c) exhibit relatively flatter *T*–*z* slopes, with individual intervals showing EI values exceeding 1, specifically, WC5 in Fig. 10(a), WC6 in Fig. 10(b), and WC4 in Fig. 10(c). In contrast, Fig. 10(d)–(g) show steeper *T*–*z* slopes and EI values mostly below 1 throughout this interval. *T*–*x* plots illustrate along-strike throw variations within the lower Wenchang Formation (Fig. 11(a)). In the F2 segment, throw values range between 3 and 13 km, with maximum displacement reaching approximately 1000 m in WC6. In comparison, the F1 segment generally displays lower throw (<780 m) and less variation along strike.

In the WC3–WC1 interval (green-shaded), Fig. 10(a)–(c) show predominantly low EI values (below 1) and steep *T*–*z* slopes. Conversely, Fig. 10(d)–(g) show localized segments with EI exceeds 1 and relatively flatter slopes, notably in Fig. 10(d)–(f). *T*–*x* plots also show relatively lower throw in the Upper Wenchang Formation (Fig. 11(b)). Throw along F2 is typically less than 280 m, while throw along F1 exceeds 450 m. Between 24 and 33 km, the throw maxima shift upward from WC3 to WC1, with maximum displacement occurring at progressively shallower intervals.

In the Enping Formation (yellow-shaded), Fig. 10(a)–(d) show EI values below 1 and progressively steeper *T*–*z* slopes upward. In contrast, Fig. 10(e)–(g) display localized intervals where EI exceeds 1, accompanied by a gradual flattening of *T*–*z* slope. *T*–*x* plots show

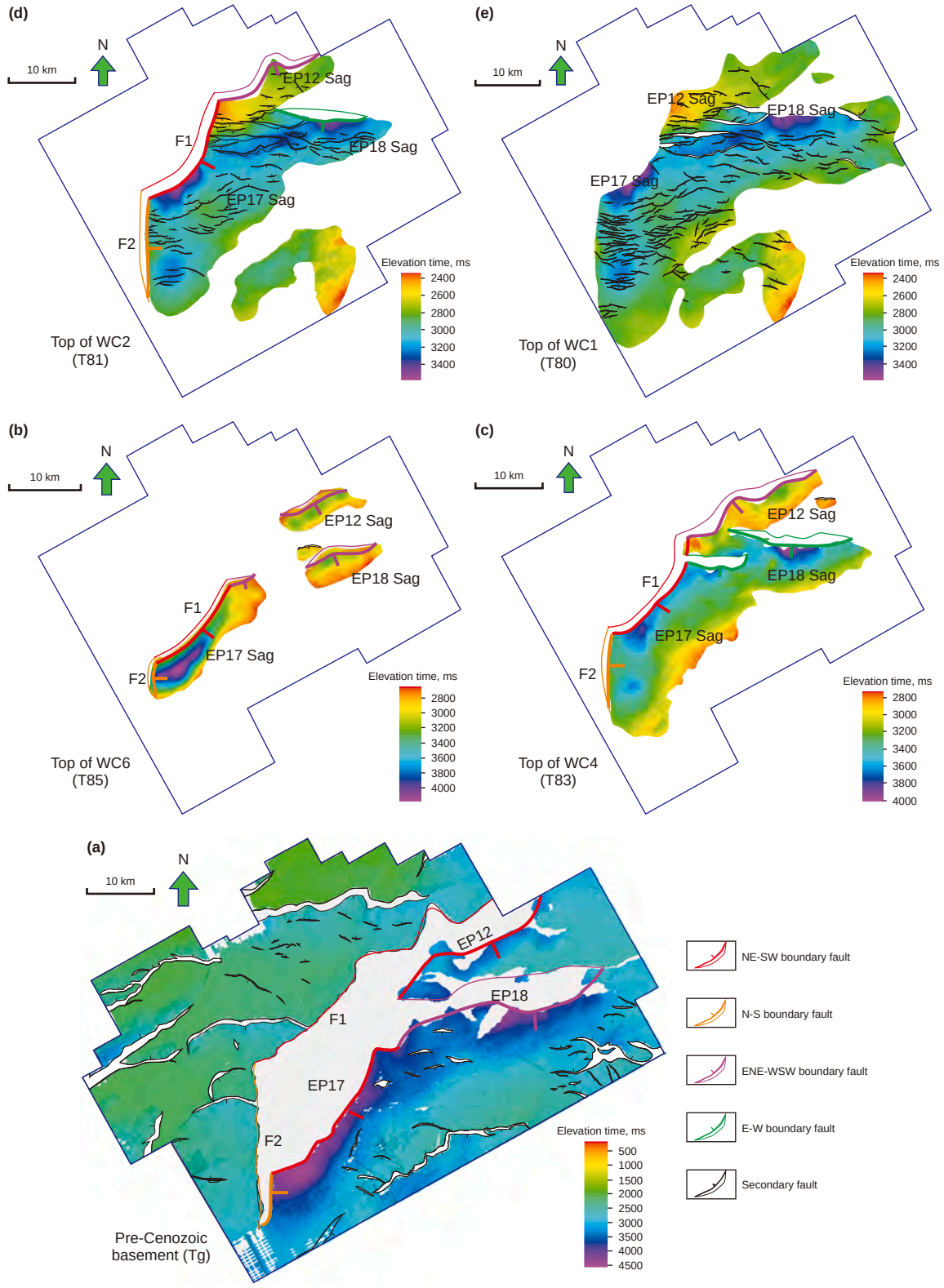

Fig. 6. Distribution of the fault system across key stratigraphic horizons in the Enping-17 Sag. **(a)** Tg (pre-Cenozoic basement), **(b)** T85 (top WC6), **(c)** T83 (top WC4), **(d)** T81 (top WC2), and **(e)** T80 (top WC1). Colored lines indicate boundary faults with different strikes, and thin black lines denote secondary faults. Interpreted fault traces at successive stratigraphic levels, illustrating variations in fault segmentation and alignment with depth.

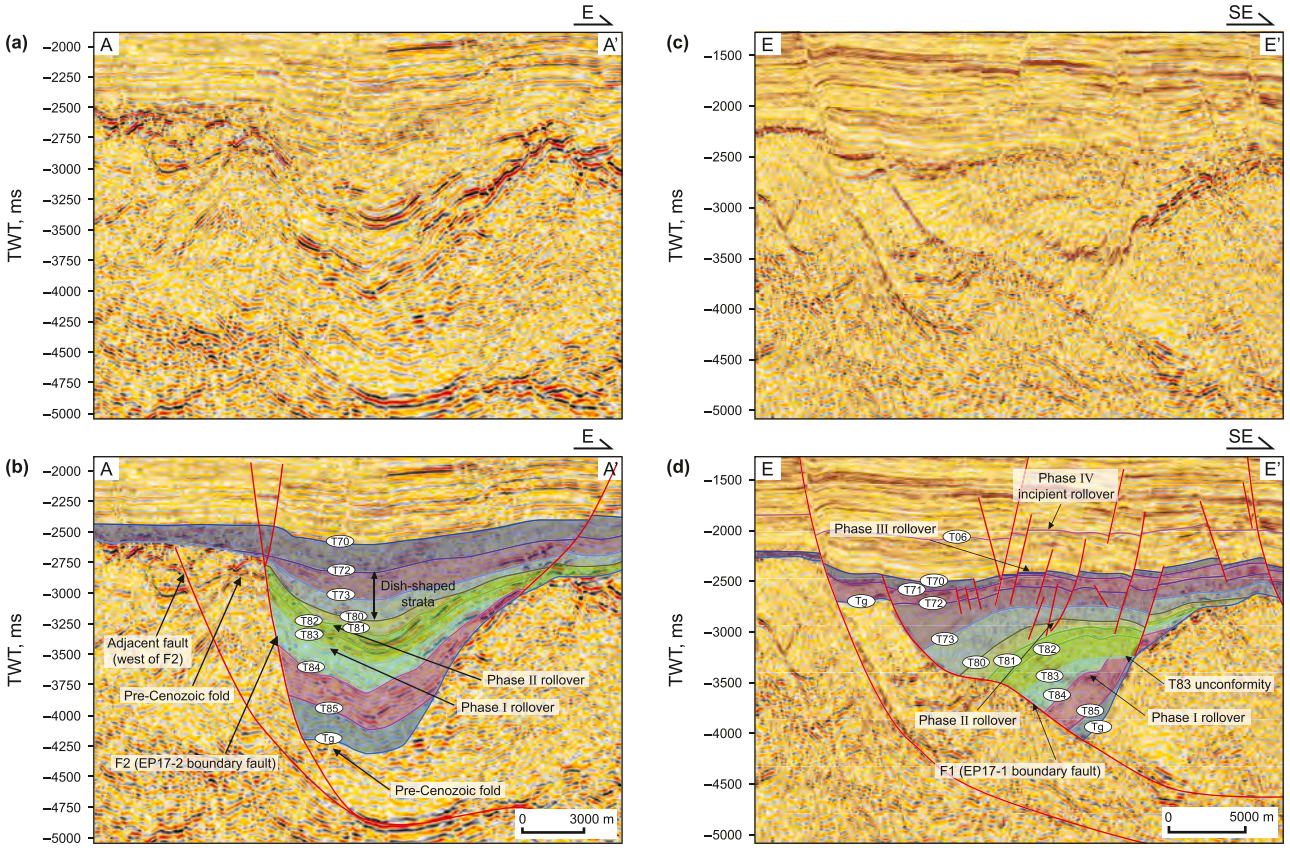

Fig. 7. Seismic profiles illustrating the geometry of boundary faults in the Enping-17 Sag. **(a)** Uninterpreted and **(b)** interpreted seismic sections showing the characteristics of Fault F2 and an adjacent fault to its west in the southern parts of the Enping-17 Sag. **(c)** Uninterpreted and **(d)** interpreted seismic sections showing the characteristics of Fault F1 in the northern parts of the Enping-17 Sag (See Fig. 1(b) for location). Colored intervals correspond to the Wenchang Formation, subdivided into WC6 (Tg–T85), WC5 (T85–T84), WC4 (T84–T83), WC3 (T83–T82), WC2 (T82–T81), and WC1 (T81–T80), as well as the overlying Enping Formation. Minor reflectors without stratigraphic disruption are omitted for clarity.

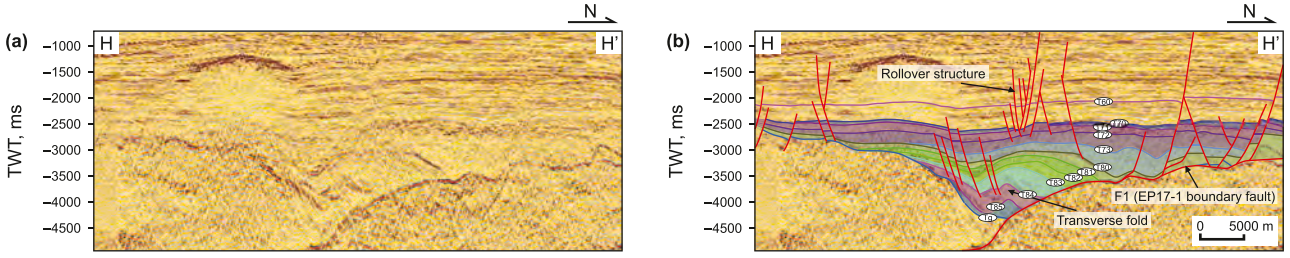

Fig. 8. Seismic profile oriented along the strike of the Enping-17 boundary fault. **(a)** Uninterpreted and **(b)** interpreted seismic sections showing transverse folds along the strike of the Enping-17 boundary fault (See Fig. 1(b) for location). Colored intervals correspond to the Wenchang Formation, subdivided into WC6 (Tg–T85), WC5 (T85–T84), WC4 (T84–T83), WC3 (T83–T82), WC2 (T82–T81), and WC1 (T81–T80), as well as the overlying Enping Formation.

an overall increase in throw compared to the Upper Wenchang Formation (Fig. 11(c)). In the F2 segment, throw values are generally below 250 m, while the F1 segment displays localized areas where throw exceeds 600 m, indicating spatial variability in throw.

4.2.2. Fault segmentation and deformation from seismic and physical models

Localized reductions in fault throw were identified at four positions along strike in the *T–x* plots (Fig. 11), occurring at approximately 3.7, 12.7, 18.4, and 24.2 km. These throw anomalies span multiple stratigraphic intervals and are most obvious in the lower Wenchang Formation (WC6–WC4) at points 1 and 2 (Fig. 11(a)), in the Upper Wenchang Formation (WC3–WC1) at point 3 (Fig. 11(b)), and in the Enping Formation at point 4 (Fig. 11(c)).

To further examine the structural context of these throw variations, the corresponding positions were compared across four fault surface attribute maps derived from the 3D model: elevation time, dip angle, dip azimuth, and generalized slip tendency (Fig. 12). Points 2, 3, and 4 correspond to local changes in dip angle, dip azimuth, or slip tendency, while point 1 shows no prominent geometric irregularity. These spatial comparisons provide a geometric basis for interpreting throw distribution patterns along strike.

In addition to localized observations, systematic differences are evident between F1 and F2 across all fault surface attribute models

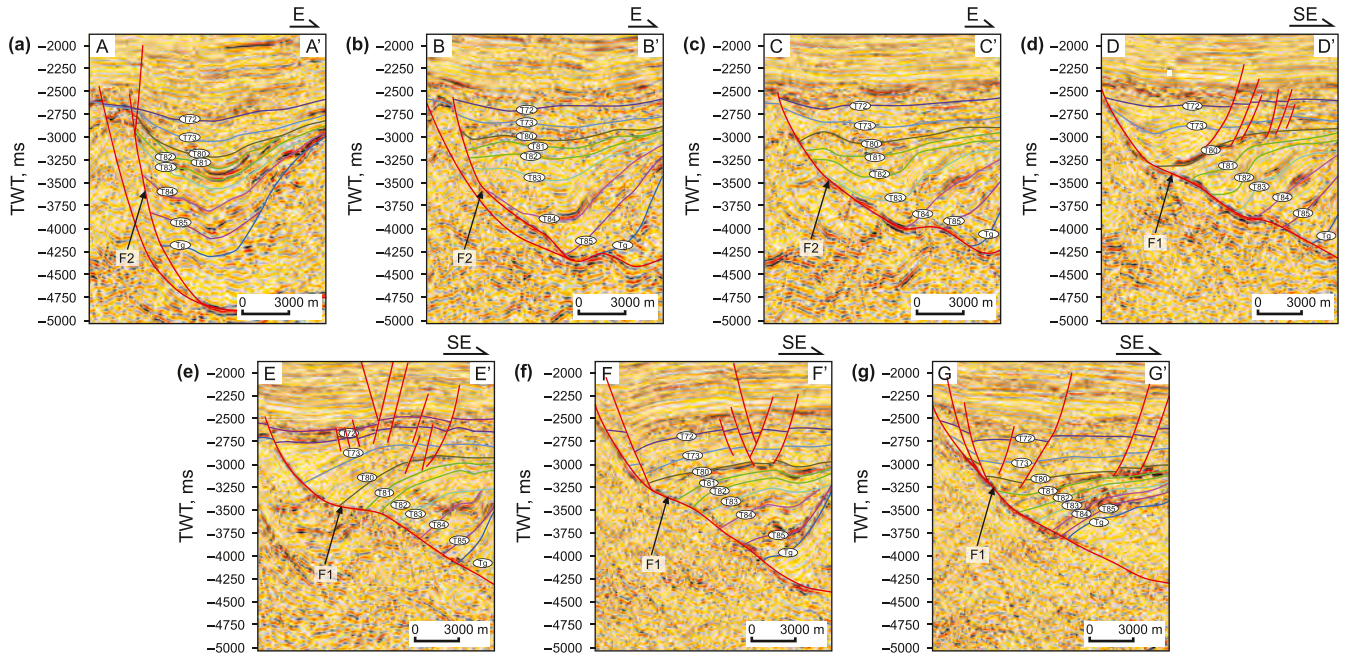

Fig. 9. Representative seismic sections across the Enping-17 sag-controlling boundary fault, illustrating the characteristics of F1 and F2 as well as stratigraphic variations. **(a)–(g)** Correspond to locations shown in Fig. 1(b). T80 = top of WC1, T81 = WC2, T82 = WC3, T83 = WC4, T84 = WC5, T85 = WC6.

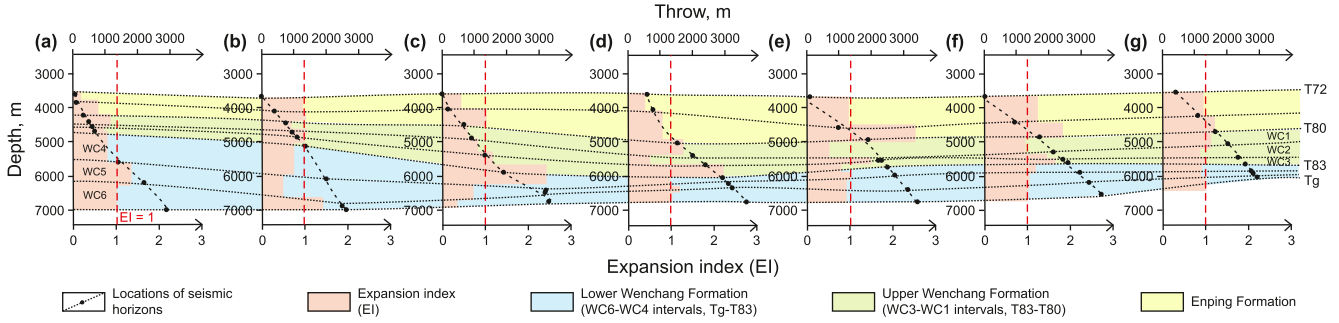

Fig. 10. *T–z* plots and EI values for the Enping-17 boundary fault during the syn-rift stage, derived from seven representative seismic profiles nearly perpendicular to the fault (Fig. 9(a)–(g)). Profile locations are indicated in Fig. 1(b). The blue shaded intervals correspond to WC6, WC5, and WC4, and the green shaded intervals correspond to WC3, WC2, and WC1 (from bottom to top).

(Fig. 12). In the elevation time model (Fig. 12(a)), F2 corresponds to greater two-way travel times, ranging from approximately −3250 to −4750 ms. In contrast, F1 displays shallower depths (−2750 to −3750 ms) and a smoother gradient along strike. In the dip angle map (Fig. 12(b)), F2 shows consistently steeper dips, typically between 45° and 55°, whereas F1 maintains gentler dips around 25°–30°. In the dip azimuth map (Fig. 12(c)), F2 exhibits values ranging between 75° and 100°, corresponding to a generally N–S-oriented geometry, while F1 shows values between 125° and 140°, reflecting a NE-trending orientation. The slip tendency map (Fig. 12(d)) shows that F2 has higher values, reaching 0.07 to 0.08, compared to the more moderate and spatially uniform values of 0.03–0.05 along F1. Overall, F2 is characterized by greater depth, steeper dips, and more variable structural attributes, whereas F1 appears shallower, gently dipping, and structurally more coherent. Additionally, a steep fault west of F2 (previously mentioned in Fig. 7(b)) is also visible in the 3D model. It does not clearly deform the overlying sedimentary layers and is noted here as a possible pre-existing structure for further discussion.

To complement the seismic observations, physical modeling under NW–SE-directed extension was carried out. The resulting map-view images document surface deformation at successive stages of extension. These observations are presented in the following section.

The initial model incorporated NE–SW-trending and N–S-trending basement structures, which were predefined in the PDMS layer (schematically shown in Fig. 4). These structures are not visible at the surface prior to deformation due to coverage by the overlying sand layer. At an early stage of deformation (5 mm extension), a subtle N–S-trending surface fracture became visible in the southern part of the model (Fig. 13(b)). This feature was located above the position of the predefined N–S basement structure. With increased extension to 15 mm, the N–S-trending fracture extended laterally in the southern part of the model (Fig. 13(c)). A shallow NE–SW-trending fracture was also observed in the northern area, aligned with the position of the predefined NE-trending structure. Between the two features, marker lines became curved and discontinuous, showing visible geometric distortion.

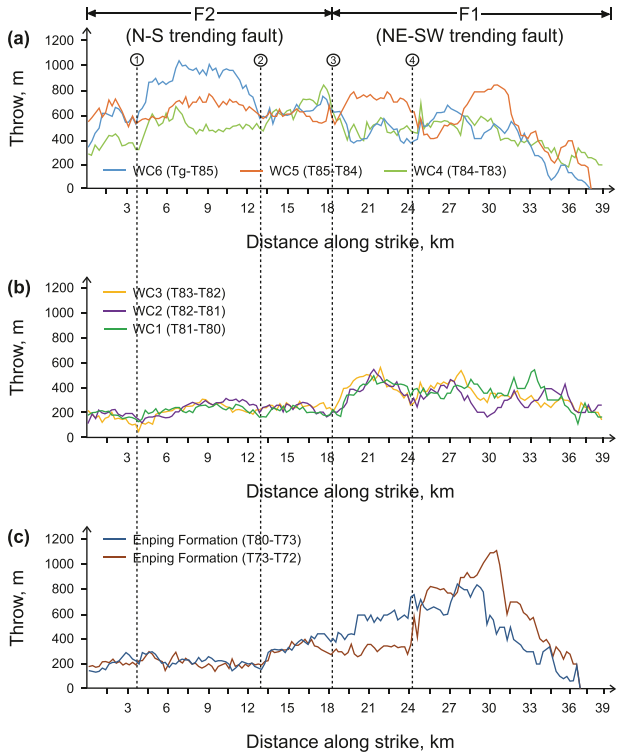

Fig. 11. *T–x* plots of the Enping 17 boundary fault (the entire length of F1 and F2): **(a)** Lower Wenchang Formation (including WC6 to WC4); **(b)** Upper Wenchang Formation (including WC3 to WC1); **(c)** Enping Formation. The sampling interval is 0.2%–0.5% of the total fault length.

At 21.6 mm extension, the NE–SW-trending fracture continued to propagate toward the center of the model. In the southern part, the N–S-trending fracture extended further north. Between the two features, marker lines appeared offset and discontinuous, and surface fractures began to merge, forming a visibly curved trace (Fig. 13(d)). By 26.8 mm of extension, the NE–SW-trending and N–S-trending fracture appeared to have linked at the surface, forming a geometrically continuous, composite fracture zone. The northern segment continued to propagate northeastward, accompanied by increased marker offset, while the southern segment showed limited additional rupture (Fig. 13(e)).

At 28.6 mm extension, this composite fracture zone further expanded, particularly in the northern segment, where fracture width and marker line offset increased significantly. The southern segment remained relatively stable, with only limited surface changes (Fig. 13(f)). These observations document spatial differences in surface deformation patterns under NW–SE-directed extension. Map-view images and sequential deformation stages illustrate that initially discrete fault traces became connected, forming composite fault zones that exhibit significant lateral continuity, with no observable strike-slip motion.

5. Discussion

5.1. Fault reactivation under multiphase extension

The Enping-17 boundary fault system exhibits significant spatial and temporal variations in geometry and displacement, as revealed by seismic interpretation, 3D fault attribute models, and physical experiments. Some segments display consistent orientations and early displacement, suggesting possible reactivation of

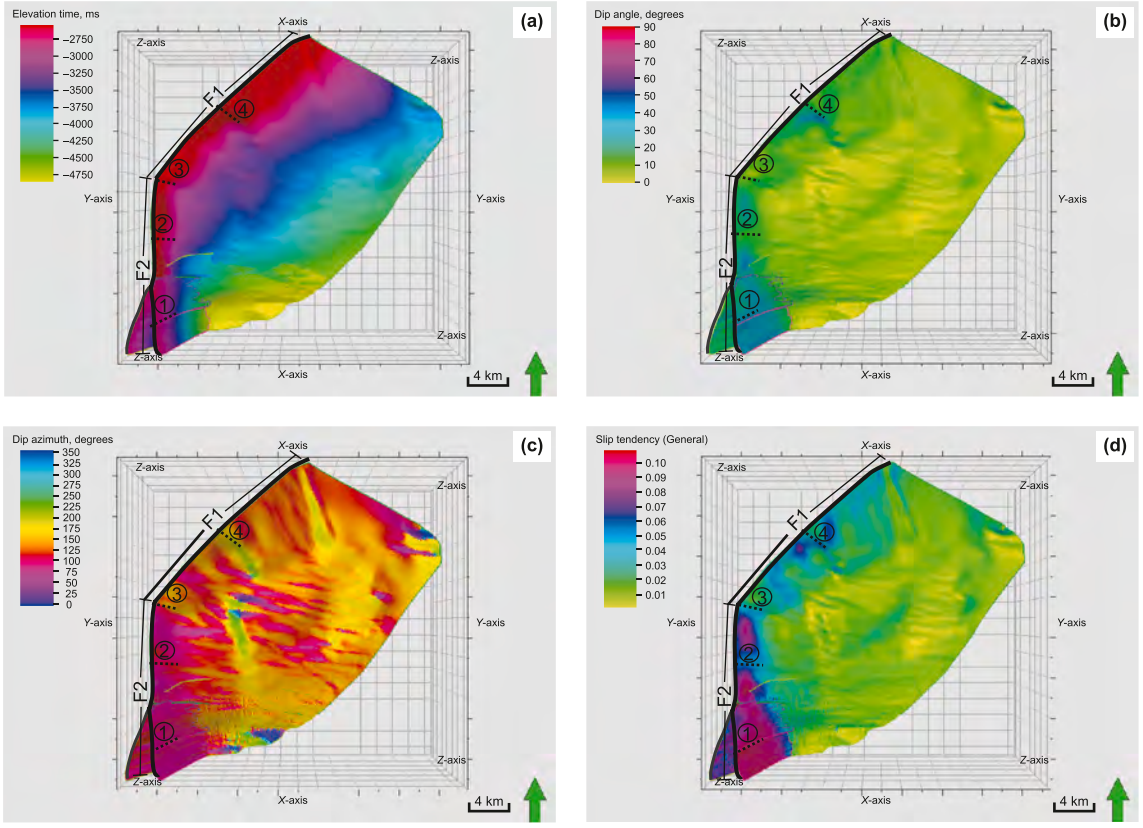

Fig. 12. Fault surface attributes of the Enping-17 boundary fault derived from seismic interpretation: **(a)** elevation time, ms; **(b)** dip angle, °; **(c)** dip azimuth, °; and **(d)** generalized slip tendency. F1 (22 km) and F2 (17 km) are shown in bold black lines. A steep fault west of F2 is also visible. Numbers 1–4 mark positions corresponding to localized throw minima identified in Fig. 10.

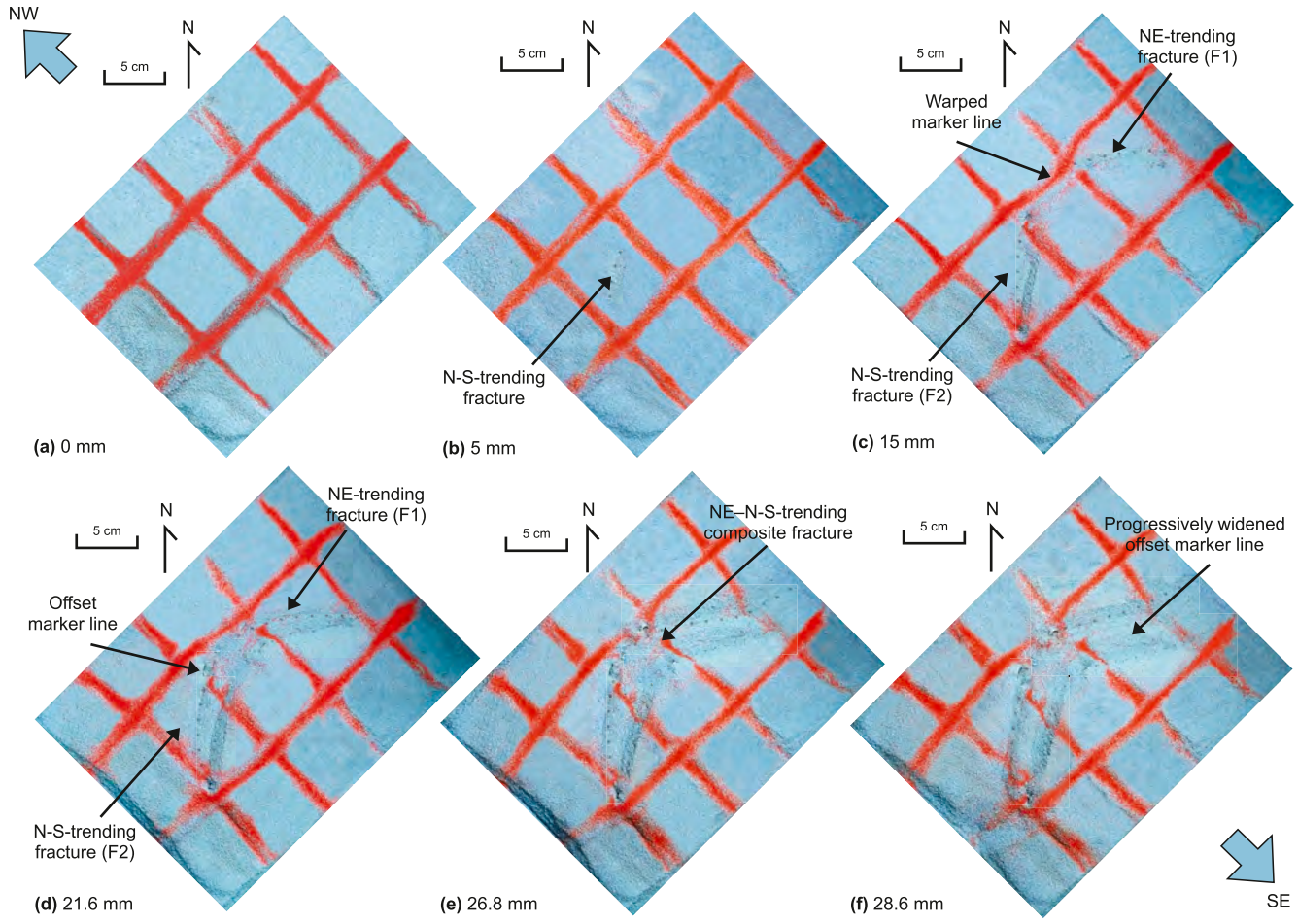

Fig. 13. Experimental results showing surface deformation patterns during NW–SE-directed extension: **(a)** 0 mm, **(b)** 5 mm, **(c)** 15 mm, **(d)** 21.6 mm, **(e)** 26.8 mm, and **(f)** 28.6 mm of extension. Dashed lines mark inferred surface traces of deformation based on marker offset and surface irregularities. Predefined weak zones were introduced into the PDMS base prior to sand deposition and are not visible at the surface.

pre-existing faults during the initial rifting phase, although direct evidence for structural inheritance remains limited. In this study, multiphase extension refers to three successive episodes: an initial NW–SE extension during early Wenchang (Rift Ia), an NNW–SSE phase in late Wenchang (Rift Ib), and a final N–S extension in the Enping stage (Ye et al., 2018a, 2020; Peng et al., 2022). The following sections examine fault reactivation patterns, timing, and mechanical implications under evolving stress regimes, with a focus on distinguishing inherited from newly formed faults.

However, several limitations should be acknowledged when interpreting the reactivation processes and structural implications of the Enping-17 boundary fault system. Although seismic data provides valuable geometric and kinematic insights, resolution decreases with depth, potentially obscuring small-scale features or early displacement signals. The identification of inherited structures remains partly interpretive due to limited exposure of pre-Cenozoic basement fabrics and the lack of direct chronological constraints on fault initiation. Moreover, while physical experiments illustrate plausible reactivation patterns under idealized conditions, the simplifications may limit the ability to fully represent the complexity of natural fault systems, particularly in scaling and material properties.

5.1.1. Fault reactivation: evidence and mechanisms

Inactive pre-existing structures are rare in the Enping-17 Sag, which may reflect both tectonic and data-related factors. Multiphase extension could have favored the reactivation of many basement anisotropies, while poor basement imaging obscures smaller non-reactivated features. Because of limited seismic resolution, quantitative activity parameters such as slip rates or EI values cannot be derived for pre-Cenozoic structures. Instead, we rely on indirect but widely accepted criteria, including geometric alignment with basement fabrics, evidence of early displacement on throw-depth profiles, and orientations oblique to the main syn-rift extension (Bonini et al., 2012; Ye et al., 2018a; Phillips et al., 2019; Strugale et al., 2021; Samsu et al., 2023; Ji et al., 2025). These observations highlight the potential role of inherited fabrics, which is examined further through the contrasting behavior of F1 and F2.

Within this structural framework, F1 shows a consistent NE–SW orientation and a relatively low dip angle of 25°–30° (Fig. 12(b) and (c)), with a laterally continuous trace and a steep-flat-steep (S-shaped) vertical profile (Fig. 7(d)). In the *T–z* and *T–x* plots, F1 displays limited displacement in early syn-rift stage (WC6–WC4), followed by a marked increase during the later stages (WC3–EP) (Figs. 10 and 11). These features deviate from typical high-angle extensional faults and instead suggest reactivation along a mechanically favorable, low-angle inherited surface. Although direct evidence of thrust-related deformation is lacking in the Enping-17 Sag, similar low-angle normal faults (<30°) in other rift systems, such as the North Sea and Apennines, have been widely interpreted as extensional reactivations of earlier

compressional faults (Ghisetti and Vezzani, 1999; Collettini and Sibson, 2001; Fernández-Blanco et al., 2019). The smooth, well-connected fault surface observed in 3D models (Fig. 12), combined with its progressive activation, supports a plausible inherited origin for F1 under the prevailing extensional regime.

In contrast, F2 trends nearly N–S with a steeper dip angle (45°–55°) and a segmented trace (Fig. 12(b) and (c)). F2 exhibits significant displacement during the early syn-rift stage (WC6–WC4), followed by a progressive decline in the subsequent stages (Figs. 10 and 11). In 3D models, F2 is characterized by irregular bifurcation and localized discontinuities (Fig. 12), deviating from the smoother geometry of F1. These characteristics suggest that F2 did not evolve as a single coherent structure, but rather developed within a structurally heterogeneous zone. It is plausible that faulting was localized along mechanically weak segments, some of which may coincide with nearby pre-existing basement features. Supporting this interpretation, a subvertical fault located west of F2 penetrates into the basement, yet lacks any evidence of syn-rift displacement (Fig. 7(b)), offering a useful reference for non-reactivated inherited structures.

The contrasting activation patterns of F1 and F2 reflect differences in their geometric compatibility with the early extensional stress regime. Fault dip and orientation fundamentally influence stress distribution: under extensional regimes, shear stress peaks near 45° dip while effective normal stress declines toward steeper dips, placing high-angle faults closer to the Coulomb failure envelope (Fig. 14) (Zoback and Townend, 2001; Moeck et al., 2009; Taghipour et al., 2019; Webber et al., 2022). Additionally, faults whose strike forms an acute angle (<45°) with the extension direction are more prone to reactivation, as shown in centrifuge experiments (Zou et al., 2024).

These mechanical principles explain the earlier activity of F2, whose steep dip and N–S-trending aligned favorably with the NW–SE extension. Its segmented geometry and early displacement suggest strain localization along mechanically weak zones. In contrast, although the low-angle, NE–SW-trending F1 was initially less favorably oriented, it shows evidence of progressive reactivation along a smooth, inherited surface as extension continued. This interpretation is supported by slip tendency analysis (Fig. 12(d)), indicating higher failure potential along F2. The activation contrast reflects combined controls of dip, strike, inherited anisotropy, and local strain accommodation. Such factors have been widely recognized in both physical models and rift systems to govern selective reactivation of pre-existing faults (Henza et al., 2011; Tong and Yin, 2011; Zwaan and Schreurs, 2017; Fernández-Blanco et al., 2019).

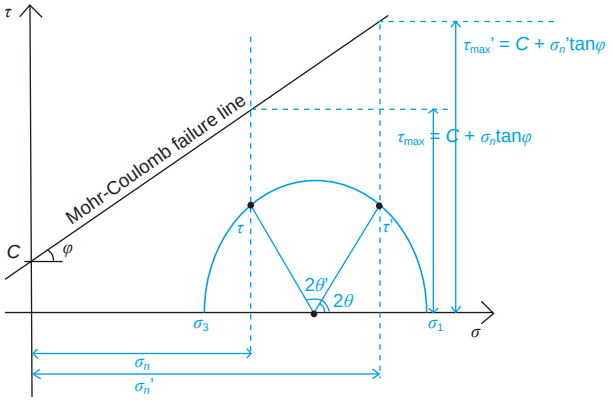

Fig. 14. The Mohr-circle diagram illustrating fault slip tendency at different dip angles. Shear stress (τ) on low-angle faults (θ) plots farther from the Coulomb failure envelope, while τ' for high-angle faults (θ') lies closer to the envelope, indicating a greater likelihood of activation (modified from Van den Bogert and Van Eijs, 2020).

5.1.2. Segment linkage and activity evolution of boundary faults

The regional extensional stress field in the northern South China Sea underwent a progressive clockwise rotation during the Paleogene, shifting from NW–SE to N–S (Wang et al., 2015; Wu et al., 2016; Ye et al., 2018b). This evolving stress regime offers a useful framework to evaluate how boundary faults in the Enping-17 Sag responded through time. In particular, the activity of the two boundary faults exhibited notable divergence across different rift stages, suggesting a possible link between evolving stress orientations and fault reactivation behavior.

T–x plots show a sharp drop in displacement at WC6 along F2 (Fig. 11(a)), indicating an abrupt transfer of throw across segments. Localized transverse fold is observed in WC5 strata (Fig. 8(b)), suggesting mechanical interaction during deformation. Physical modeling under uniform boundary conditions replicates this behavior, showing rapid merging of initially separate fault segments shortly after the onset of extension (Fig. 13(c) and (d)). Additionally, 3D structural models reveal a smooth vertical transition between F1 and F2 despite their distinct strikes, consistent with a composite fault system (Fig. 12). Multiple lines of evidence indicate that geometric and mechanical connection between F1 and F2 was likely established during the initial phase of the early Wenchang stage (especially in WC6–WC5 intervals), even as their subsequent kinematic evolution remained distinct.

Seismic profiles reveal thicker lower Wenchang Formation strata adjacent to F2 (Fig. 7(b)–(d)), while *T–z* and *T–x* plots indicate greater displacement along this fault during the early Wenchang stage (Rift Ia) (Figs. 10(a) and (b) and 11(a)). In physical modeling, deformation first appeared along F2 (Fig. 13(b)), confirming its earlier activation relative to F1 during the onset of rifting. From the late Wenchang stage (Rift Ib) onward, a progressive shift in fault activity became apparent. *T–x* plots show a steady increase in displacement along F1, while displacement along F2 declined and eventually stagnated (Fig. 11). This transition is also captured in the *T–z* plots: displacement curves for F1 flatten progressively through the Upper Wenchang and Enping formations (Fig. 10(e)–(g)), whereas those for F2 remain steep. Seismic profiles further confirm these trends, with F1 bounding increasingly thicker syn-rift successions in later stages (Fig. 7(b) and (d)).

From WC6 to WC2, the along-strike length of F1 increased by 12.4 km, substantially more than the 4.5 km observed for F2 (Fig. 6(b)–(d)). This trend is mirrored in stratigraphic throw distributions, with F2 showing higher values during WC6–WC4 (Fig. 15(a)–(c)), and F1 becoming increasingly dominant in subsequent intervals (Fig. 15(e)–(g)). These patterns indicate that fault reactivation was governed not solely by geometric linkage, but by evolving fault-stress compatibility. As the extensional stress field rotated clockwise from NW–SE to N–S, F1's NE–SW orientation became progressively more aligned with the principal extension direction, while F2's N–S orientation grew less favorable for slip. Similar reactivation trends driven by stress rotation have been reported in other rift systems (Agostini et al., 2011; Brune, 2014; Fernández-Blanco et al., 2019; Lou et al., 2022), highlighting the critical role of stress-fault alignment in multiphase extensional deformation.

Although strike-slip components can influence fault displacement in oblique extensional regimes, current evidence suggests such effects were limited in the Enping-17 Sag. No diagnostic strike-slip features (flower structures or lateral offsets) are observed in seismic profiles below the T72 horizon, and minor transtensional deformation is restricted to overlying strata (Fig. 8).

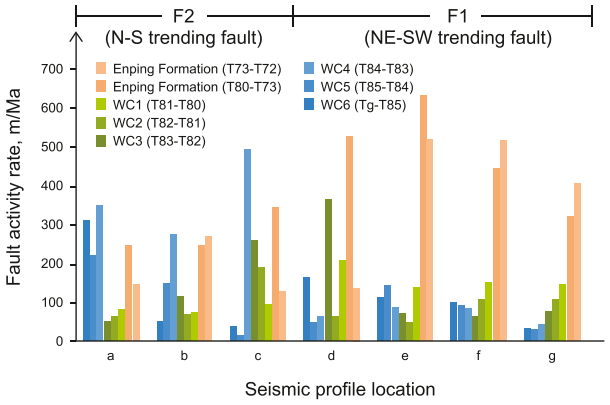

Fig. 15. Boundary fault activity of the Enping-17 Sag during the syn-rift stage, based on maximum fault activity rate along multiple fault segments with varying orientations. Derived from seven seismic profiles nearly perpendicular to the fault trace (Fig. 8(a)–(g)), with profile locations shown in Fig. 1(b).

Additionally, physical modeling under uniform extensional conditions produced predominantly dip-slip motion, even along obliquely oriented segments such as F2 (Fig. 13). These observations support that vertical displacement dominated during the main syn-rift stages, consistent with a predominantly extensional regime in the northern South China Sea (Wang et al., 2015; Deng et al., 2017; Ye et al., 2020). Accordingly, throw-based metrics such as *T*–z plots, *T*–*x* plots, and EI values remain appropriate for evaluating relative fault activity, as demonstrated in other multi-phase rift systems (Golombek et al., 1983; Withjack et al., 2017; Wang et al., 2023; Bauer et al., 2025).

5.2. Implications of pre-existing fault reactivation for sag architecture and petroleum systems

5.2.1. Differential fault reactivation and segmental evolution of the Enping-17 Sag

The northern margin of the South China Sea preserves a complex tectonic record shaped by the combined effects of Pacific subduction rollback, India–Eurasia collision, and progressive continental extension (Cullen et al., 2010; Franke et al., 2014; Peng and Li, 2024). Two primary geodynamic mechanisms: extrusion-related pull-apart extension driven by southeastward escape of the Indochina Block along the left-lateral Red River fault zone, and back-arc extension induced by slab rollback of the paleo-Pacific plate, likely operated sequentially or interacted, producing a progressive clockwise rotation of the stress field during the Cenozoic (Guo et al., 2023; Peng and Li, 2024). These tectonic processes directly influenced fault orientations in the Pearl River Mouth Basin, shifting from NE-trending faults during early extension to E–W-trending faults during later rifting (Li et al., 2014; Deng et al., 2021; Samsu et al., 2023). During the Eocene, the stress field rotated from NW to N–S, corresponding to three major tectonic phases: Zhuqiong I (49–43 Ma), Huizhou (43–39 Ma), and Zhuqiong II movements (39–32 Ma). In particular, the Huizhou Movement marked a regional stress reorganization that facilitated reactivation of NE-trending basement faults and influenced fault segmentation in sags (Shi et al., 2020; Hao et al., 2021). This tectonic framework enables the Enping-17 Sag to illustrate how pre-existing fault geometries and evolving stress conditions governed the differential development of sag segments.

During the early Wenchang stage (rift Ia, 49–43 Ma), NW–SE-directed extension initiated the segmentation of the Enping-17 Sag. Among the inherited basement structures, N–S-trending weaknesses such as F2 were more favorably oriented for reactivation, leading to the formation of southern fault-bounded depocenters. Structural restoration indicates that the southern sub-sag controlled by F2 exhibited greater overall subsidence and lateral extent, with buried depth to 2000 m and length of 12.5 km, both exceeding those of the northern F1-controlled segment (1800 m depth, 10 km length) (Fig. 16(b)). Seismic and stratigraphic profiles show wedge-shaped lower Wenchang strata thickening toward F2 (Fig. 7(b)), reflecting focused subsidence and enhanced accommodation. Both structural restoration and physical modeling consistently indicate that F2 initiated faulting and subsidence earlier than F1 (Figs. 13(b) and 16(b)), highlighting the role of inherited fault orientation in controlling early rift segmentation and accommodation (Fig. 17(a) and (b)).

During the late Wenchang stage (rift Ib, 43–39 Ma), the clockwise rotation of the extensional stress field was accompanied by intensified displacement along F1. This period also saw northeastward migration of the depocenter and thickening of the Upper Wenchang Formation in the northern sub-sag (Figs. 6(d) and 16(a)). Extension along F1 increased by 8.87 km with a 29.8% rise in rate, whereas the F2-controlled southern sub-sag experienced minor contraction (−0.231 km, −0.9%) (Fig. 16(a)). These spatial and temporal patterns indicate that structural dominance shifted toward F1, reflecting evolving fault-stress compatibility under a rotating extensional regime.

During the Enping stage (rift II, 39–32 Ma), the extensional stress axis rotated further toward a near N–S orientation, promoting activity along newly formed E–W-trending faults along the northern margin of the Enping-17 Sag (Fig. 6(e)). These faults cross-cut earlier structures and enhanced extension within the northern domain, where fault F1 remained active and accumulated an additional 3.5 km (10.6%) of extension (Fig. 16(a)). In contrast, fault activity in the southern segment controlled by F2 had largely ceased, with only 45 m (0.2%) of further displacement (Fig. 16(b)). This stage marked the structural focusing of subsidence toward the north, establishing the asymmetric geometry of the sag and defining its final depocenter configuration by the end of rifting (Fig. 17(c) and (d)).

5.2.2. Structural influence on petroleum system development

Geochemical data show that the Wenchang Formation source rocks in the Enping-17 Sag are dominated by Type II kerogen, with TOC values of 1.0%–2.5%. In areas deeper than 2.4 km, R_o values exceed 1.2%, indicating effective oil generation (Bai et al., 2020; Shi et al., 2023). These mature lacustrine mudstones are concentrated in the central depocenter along the boundary faults, highlighting the role of sustained fault-controlled subsidence in providing accommodation for thick source rock accumulation. In rift basins where boundary faults grow as segments and later link, early slip creates several small sub-sags, but subsequent linkage merges them into a unified depression and establishes a long-lived depocenter favorable for thick, organic-rich mudstones. This pattern is evident in the Enping-17 Sag: during Rift I, fault activity localized subsidence into a northern depocenter adjacent to the NE-trending F1 and a southern depocenter related to the nearly N–S-trending F2. With continued extension in Rift II, renewed activity and along-strike linkage integrated these depocenters into a sag-scale depression (Fig. 18).

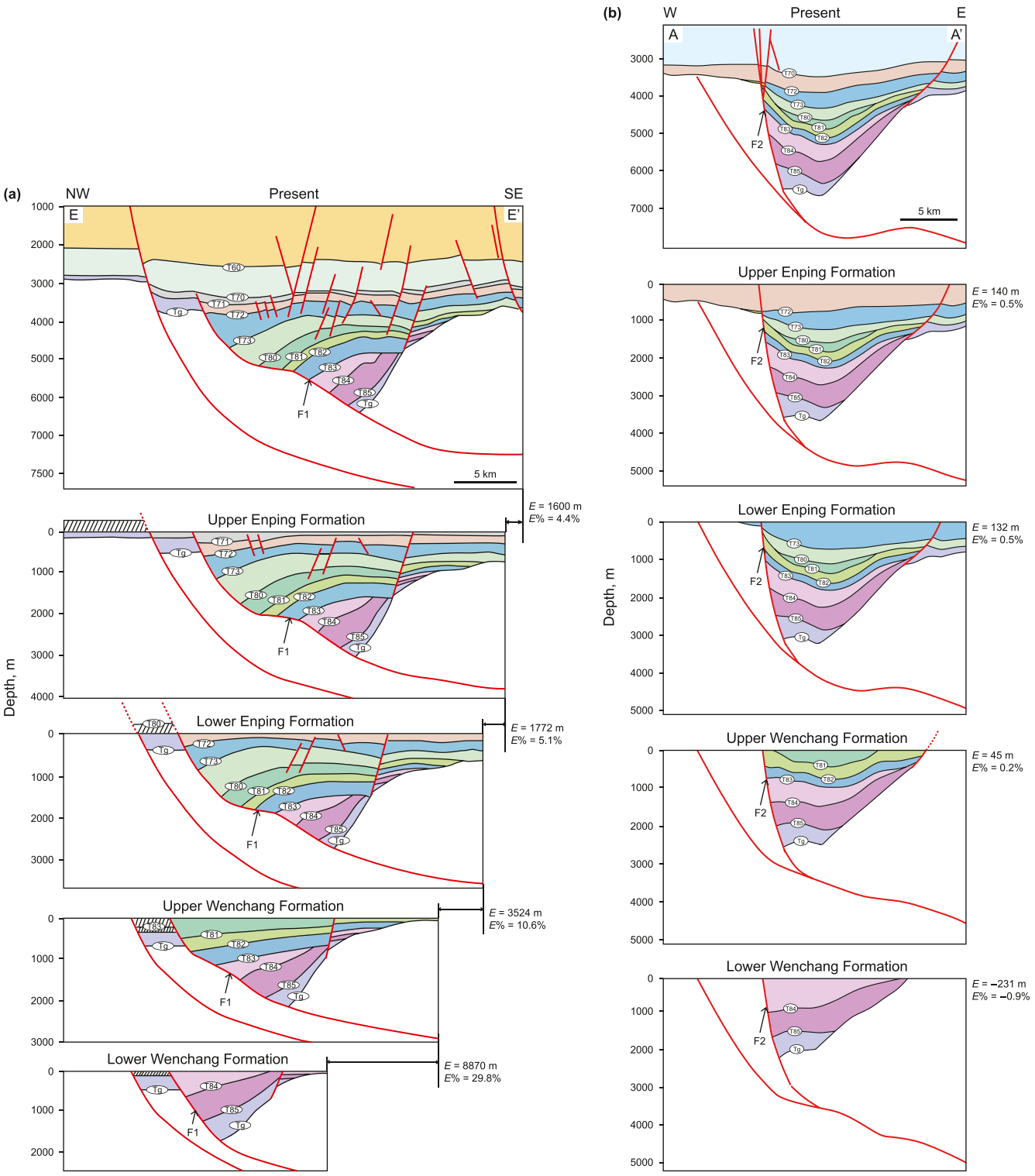

Fig. 16. Tectonic evolution of the Enping-17 Sag: **(a)** northern sub-sag evolution; **(b)** southern sub-sag evolution. *E* = extension; *E*% = extension rate. (See Fig. 1(b) for location).

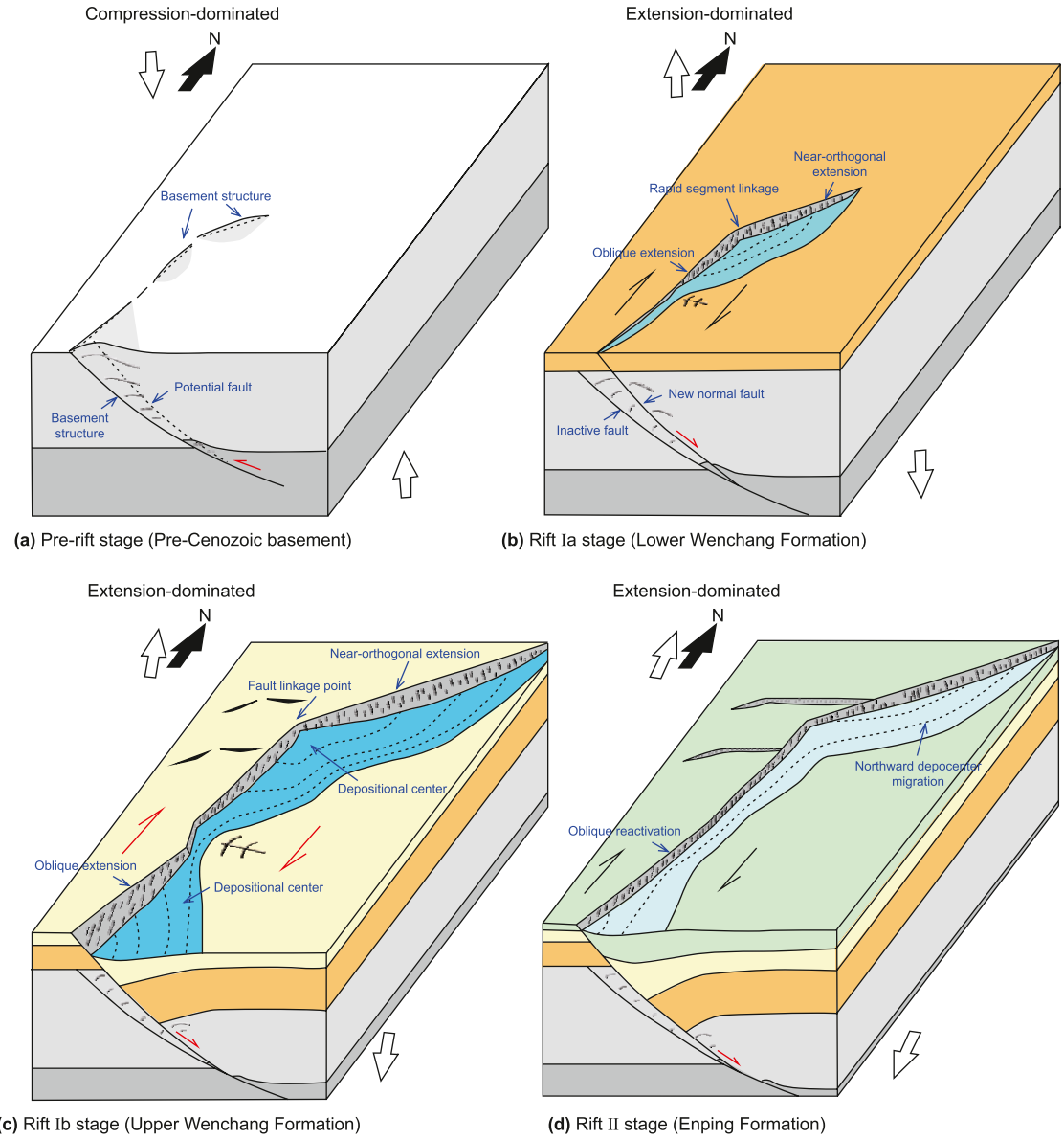

Fig. 17. Evolution of the Enping-17 Sag during different rift stages: **(a)** Pre-rift; **(b)** Rift Ia; **(c)** Rift Ib; **(d)** Rift II. Deformation primarily dip-slip under extension.

The asymmetry between the two margins reflects differences in geometry and connectivity. F1 is relatively continuous and well linked, with a smooth steep-flat-steep (S-shaped) profile that sustained stable long-term subsidence and promoted thicker, laterally extensive mid- to deep-lacustrine mudstones. In contrast, F2 is more segmented and discontinuous, partitioning subsidence into smaller, short-lived depocenters where shallow-lacustrine deposits are more common. Growth anticlines and transverse folds near linked segments (Fig. 18) further indicate sustained displacement and bending during fault interaction. Taken together, the structural contrast between F1 and F2 shows that boundary fault segmentation and linkage directly influenced sag subsidence and source rock distribution. In the Enping-17 Sag, the continuous, well-linked F1 sustained stable subsidence and favored thick mid- to deep-lacustrine mudstones, whereas the segmented F2 created smaller, short-lived depocenters dominated by shallow-lacustrine facies. Similar relationships are seen in the Northern North Sea, Campos, Santos and Pelotas basins (Contreras et al., 2010; Phillips et al., 2019; Underhill and Richardson, 2022), yet the marked asymmetry between F1 and F2 highlights how local variations in fault geometry can amplify or diminish source-rock potential within a single sag, underscoring the importance of segment-scale structural controls in petroleum system development.

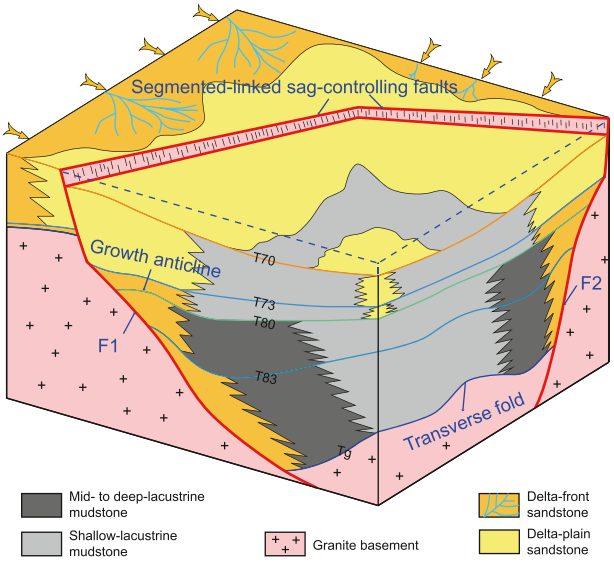

Fig. 18. 3D structural model of the Enping-17 Sag showing how segmented-linked boundary faults shaped depositional asymmetry (deep-lacustrine facies dominant along F1, shallow-lacustrine facies more widespread along F2).

6. Conclusions

(1) The northern segment of the Enping-17 Sag is characterized by the development of NE–SW-trending and ENE–WSW-trending high-angle faults, forming a step-faulted geometry with four distinct rollover phases. In contrast, the southern segment is defined by N–S-trending listric faults and exhibits only two rollover phases.

(2) N–S-trending pre-existing faults were preferentially reactivated during early NW–SE-directed extension, while NE–SW-trending and ENE-trending faults became dominant under rotated stress regimes. Their progressive linkage shaped the structural segmentation and activity evolution of boundary faults in the Enping-17 Sag.

(3) During the syn-rift evolution, the depocenter of the Enping-17 Sag progressively shifted northeastward, reflecting the temporal transition from an initially dominant southern sub-sag to a more extensive and deeper central–northeastern domain. The progressive linkage of boundary fault segments stabilized long-term subsidence and created favorable conditions for the accumulation and maturation of thick lacustrine source rocks.

(4) Fault segments with steep dips and favorable orientations relative to the early extensional stress were preferentially reactivated, while obliquely oriented or low-angle faults became active during subsequent stress rotation. This progressive reactivation order aligns with inherited fault geometries and stress orientation changes.

CRediT authorship contribution statement

Zhi-Qing Zhang: Writing – original draft, Visualization, Validation, Methodology, Investigation, Conceptualization. **Hua Liu:** Writing – review & editing, Supervision, Resources, Methodology. **Guang-Rong Peng:** Validation, Supervision, Software, Resources. **Yin Liu:** Writing – review & editing, Methodology, Conceptualization. **Zu-Lie Long:** Software, Resources, Data curation.

Declaration of competing interest

The authors declare that they have no known competing financial interests or personal relationships that could have appeared to influence the work reported in this paper.

Acknowledgements

This study was supported by the National Natural Science Foundation of China (Grant No. 42472192), and the Taishan Scholars Program of Shandong Province (Grant No. tsqn202312121). The Shenzhen Oil Company of CNOOC provided the drilling and the original 3D seismic data.

References

Agostini, A., Bonini, M., Corti, G., et al., 2011. Fault architecture in the main Ethiopian rift and comparison with experimental models: Implications for rift evolution and Nubia–Somalia kinematics. Earth Planet Sci. Lett. 301 (3–4), 479–492. https://doi.org/10.1016/j.epsl.2010.11.024.

Almqvist, B.S.G., Koyi, H., 2018. Bulk strain in orogenic wedges based on insights from magnetic fabrics in sandbox models. Geology 46 (6), 483–486. https://doi.org/10.1130/G39998.1.

Bai, Y.L., Dong, D.D., Brune, S., et al., 2019. Crustal stretching style variations in the northern margin of the South China Sea. Tectonophysics 751, 1–12. https://doi.org/10.1016/j.tecto.2018.12.012.

Bai, Y.L., Wang, X.Y., Dong, D.D., et al., 2020. Symmetry of the South China Sea conjugate margins in a rifting, drifting and collision context. Mar. Petrol. Geol. 117, 104397. https://doi.org/10.1016/j.marpetgeo.2020.104397.

Baudon, C., Cartwright, J., 2008. The kinematics of reactivation of normal faults using high resolution throw mapping. J. Struct. Geol. 30 (8), 1072–1084. https://doi.org/10.1016/j.jsg.2008.04.008.

Bauer, F., Grimmer, J.C., Houpt, L., et al., 2025. Development of intra-rift basins during stress field change in the central Upper Rhine Graben (SW Germany). Tectonics 44, e2024TC008721. https://doi.org/10.1029/2024TC008721.

Bellahsen, N., Daniel, J.M., 2005. Fault reactivation control on normal fault growth: an experimental study. J. Struct. Geol. 27 (4), 769–780. https://doi.org/10.1016/j.jsg.2004.12.003.

Bonini, M., Sani, F., Antonielli, B., 2012. Basin inversion and contractional reactivation of inherited normal faults: A review based on previous and new experimental models. Tectonophysics 522–523, 55–88. https://doi.org/10.1016/j.tecto.2011.11.014.

Bonini, M., Souriot, T., Boccaletti, M., et al., 1997. Successive orthogonal and oblique extension episodes in a rift zone: Laboratory experiments with application to the Ethiopian rift. Tectonics 16 (2), 347–362. https://doi.org/10.1029/96TC03935.

Briais, A., Patriat, P., Tapponnier, P., 1993. Updated interpretation of magnetic anomalies and seafloor spreading stages in the South China Sea: Implications for the tertiary tectonics of Southeast Asia. J. Geophys. Res. Solid Earth 98 (B4), 6299–6328. https://doi.org/10.1029/92JB02280.

Brune, S., 2014. Evolution of stress and fault patterns in oblique rift systems: 3-D numerical lithospheric-scale experiments from rift to breakup. G-cubed 15, 3392–3415. https://doi.org/10.1002/2014GC005446.

Cai, G.F., Peng, G.R., Wu, J., et al., 2022. Tectonic deformation and sedimentary filling response of the detachment faulted depression in the shallow water shelf area of the Pearl River Mouth Basin: A case study of the Enping Sag. Earth Sci. 47 (7), 2391–2409 (in Chinese).

Cao, J.H., Xia, S.H., Sun, J.L., et al., 2014. Comparison of fault structure characteristics in the northern Pearl River Mouth Basin and its geological implication. Prog. Geophys. 29 (5), 2364–2369. https://doi.org/10.6038/pg20140555.

Chen, J.J., He, D.F., Tian, F.L., et al., 2022. Control of mechanical stratigraphy on the stratified style of strike-slip faults in the central Tarim Craton, NW China. Tectonophysics 830, 229307. https://doi.org/10.1016/j.tecto.2022.229307.

Collettini, C., Sibson, R.H., 2001. Normal faults, normal friction? Geology 29 (10), 927–930. https://doi.org/10.1130/0091-7613(2001)029<0927:NFNF>2.0.CO;2.

Contreras, J., Zühlke, R., Bowman, S., et al., 2010. Seismic stratigraphy and subsidence analysis of the southern Brazilian margin (Campos, Santos and Pelotas basins). Mar. Petrol. Geol. 27 (9), 1952–1980. https://doi.org/10.1016/j.marpetgeo.2010.06.007.

Cullen, A., Reemst, P., Henstra, G., et al., 2010. Rifting of the South China Sea: New perspectives. Pet. Geosci. 16 (3), 273–282. https://doi.org/10.1144/1354-079309-908.

Cultrera, F., Barreca, G., Scarfì, L., et al., 2015. Fault reactivation by stress pattern reorganization in the Hyblean foreland domain of SE Sicily (Italy) and seismotectonic implications. Tectonophysics 661, 215–228. https://doi.org/10.1016/j.tecto.2015.08.043.

Del Ventisette, C., Bonini, M., Agostini, A., et al., 2019. Using different grain-size granular mixtures (quartz and K-feldspar sand) in analogue extensional models. J. Struct. Geol. 129, 103888. https://doi.org/10.1016/j.jsg.2019.103888.
Deng, C., Fossen, H., Gawthorpe, R.L., et al., 2017. Influence of fault reactivation during multiphase rifting: The Oseberg area, northern North Sea rift. Mar. Petrol. Geol. 86, 1252–1272. https://doi.org/10.1016/j.marpetgeo.2017.07.025.
Deng, C., Zhu, R.X., Han, J.H., et al., 2021. Impact of basement thrust faults on low-angle normal faults and rift basin evolution: A case study in the Enping sag, Pearl River Basin. Solid Earth 12 (10), 2327–2350. https://doi.org/10.5194/se-12-2327-2021.
Dooley, T.P., Schreurs, G., 2012. Analogue modelling of intraplate strike-slip tectonics: A review and new experimental results. Tectonophysics 574–575, 1–71. https://doi.org/10.1016/j.tecto.2012.05.030.
Duan, L., Meng, Q.R., Wu, G.L., et al., 2020. Nanpanjiang Basin: A window on the tectonic development of south China during Triassic assembly of the southeastern and eastern Asia. Gondwana Res. 78, 189–209. https://doi.org/10.1016/j.gr.2019.08.009.
Dubois, A., Odonne, F., Massonnat, G., et al., 2002. Analogue modelling of fault reactivation: Tectonic inversion and oblique remobilisation of grabens. J. Struct. Geol. 24 (11), 1741–1752. https://doi.org/10.1016/S0191-8141(01)00129-8.
Fernández-Blanco, D., de Gelder, G., Lacassin, R., et al., 2019. A new crustal fault formed the modern Corinth Rift. Earth Sci. Rev. 199, 102919. https://doi.org/10.1016/j.earscirev.2019.102919.
Franke, D., Savva, D., Pubellier, M., et al., 2014. The final rifting evolution in the South China Sea. Mar. Petrol. Geol. 58, 704–720. https://doi.org/10.1016/j.marpetgeo.2013.11.020.
Gabrielsen, R.H., Sokoutis, D., Willingshofer, E., et al., 2016. Fault linkage across weak layers during extension: An experimental approach with reference to the Hoop fault Complex of the SW Barents Sea. Pet. Geosci. 22 (2), 123–135. https://doi.org/10.1144/petgeo2015-029.
Gawthorpe, R.L., Leeder, M.R., 2000. Tectono-sedimentary evolution of active extensional basins. Basin Res. 12 (3–4), 195–218. https://doi.org/10.1111/j.1365-2117.2000.00121.x.
Ge, J.W., Zhu, X.M., Zhao, X.M., et al., 2020. Tectono-sedimentary signature of the second rift phase in multiphase rifts: A case study in the Lufeng Depression (38–33.9 Ma), Pearl River Mouth Basin, South China Sea. Mar. Petrol. Geol. 114, 104218. https://doi.org/10.1016/j.marpetgeo.2020.104218.
Ghisetti, F., Vezzani, L., 1999. Depth and modes of Pliocene–Pleistocene crustal extension of the Apennines (Italy). Terra Nova 11, 67–72. https://doi.org/10.1046/j.1365-3121.1999.00227.x.
Giba, M., Walsh, J.J., Nicol, A., 2012. Segmentation and growth of an obliquely reactivated normal fault. J. Struct. Geol. 39, 253–267. https://doi.org/10.1016/j.jsg.2012.01.004.
Golombek, M.P., McGill, G.E., Brown, L., 1983. Tectonic and geologic evolution of the Espanola Basin, Rio Grande Rift: Structure, rate of extension, and relation to the state of stress in the Western United States. Tectonophysics 94 (1–4), 483–507. https://doi.org/10.1016/0040-1951(83)90031-8.
Gomes, C.J.S., 2013. Investigating new materials in the context of analog-physical models. J. Struct. Geol. 46, 158–166. https://doi.org/10.1016/j.jsg.2012.09.013.
Gomes, C.J.S., Caldeira, J.N.D.M., 2011. The frictional properties of quartz sands (natural and colored): measurements from analogue experiments and from a ring-shear tester. REM: Rev. Esc. Minas. 64 (3), 289–298. https://doi.org/10.1590/S0370-44672011000300006.
Guo, B.W., Yu, F.S., Li, H., 2023. Structural evolution and mechanism of multi-phase rift basins: A case study of the Panyu 4 Sag in the Zhu I Depression, Pearl River Mouth Basin, South China Sea. Front. Earth Sci. 11, 1103827. https://doi.org/10.3389/feart.2023.1103827.
Hall, R., 2012. Late Jurassic–Cenozoic reconstructions of the Indonesian region and the Indian Ocean. Tectonophysics 570–571, 1–41. https://doi.org/10.1016/j.tecto.2012.04.021.
Hao, S.S., Mei, L.F., Shi, H.S., et al., 2021. Rift migration and transition during multiphase rifting: insights from the proximal domain, northern South China Sea rifted margin. Mar. Petrol. Geol. 123, 104729. https://doi.org/10.1016/j.marpetgeo.2020.104729.
He, J.H., Wu, J., Bai, H.J., et al., 2022. Hydrocarbon migration patterns along faults in the Enping Sag, Pearl River Mouth Basin. Mar. Geol. Front. 38 (8), 55–66. https://doi.org/10.16028/j.1009-2722.2021.138 (in Chinese).
Henza, A.A., Withjack, M.O., Schlische, R.W., 2010. Normal-fault development during two phases of non-coaxial extension: An experimental study. J. Struct. Geol. 32 (11), 1656–1667. https://doi.org/10.1016/j.jsg.2009.07.007.
Henza, A.A., Withjack, M.O., Schlische, R.W., 2011. How do the properties of a pre-existing normal-fault population influence fault development during a subsequent phase of extension? J. Struct. Geol. 33 (9), 1312–1324. https://doi.org/10.1016/j.jsg.2011.06.010.
Hu, Y., 2019. Cenozoic basin structures and their genetic evolution in the Zhu I Depression, Pearl River Mouth Basin. Acta Geol. Univ. Pekin. 25 (1), 81–92. https://doi.org/10.16108/j.issn1006-7493.2018114 (in Chinese).
Huang, C., Zhou, D., Sun, Z., et al., 2005. Deep crustal structure of Baiyun Sag, northern South China Sea revealed from deep seismic reflection profile. Chin. Sci. Bull. 50, 1131–1138. https://doi.org/10.1360/04wd0207.
Huang, H.B., Qiu, X.L., Pichot, T., et al., 2019. Seismic structure of the northwestern margin of the South China Sea: Implication for asymmetric Continental extension. Geophys. J. Int. 218 (2), 1246–1261. https://doi.org/10.1093/gji/ggz219.
Hui, G.G., Li, S.Z., Guo, L.L., et al., 2021. A review of geohazards on the northern continental margin of the South China Sea. Earth Sci. Rev. 220, 103733. https://doi.org/10.1016/j.earscirev.2021.103733.
Hui, G.G., Li, Z.G., Wang, W.T., et al., 2022. Characteristics of fault systems on the northern shelf of the South China Sea and their implications for the opening of the South China Sea. Geotect. Metallogenia 46 (3), 501–516. https://doi.org/10.16539/j.ddgzyckx.2022.03.007 (in Chinese).
Jackson, C.A.L., Rotevatn, A., 2013. 3D seismic analysis of the structure and evolution of a salt-influenced normal fault zone: A test of competing fault growth models. J. Struct. Geol. 54, 215–234. https://doi.org/10.1016/j.jsg.2013.06.012.
Ji, K., Deng, C., Li, B., et al., 2025. Spatiotemporal variations and genetic mechanisms of Cenozoic rift development in the Pearl River Mouth Basin. Geol. Sci. Technol. Inf. https://doi.org/10.19509/j.cnki.dzkq.tb20240054 (in press) (in Chinese).
Keep, M., McClay, K.R., 1997. Analogue modelling of multiphase rift systems. Tectonophysics 273 (3–4), 239–270. https://doi.org/10.1016/S0040-1951(96)00272-7.
Kim, I.H., Park, S.I., Kang, N.K., et al., 2023. Role of inherited fault reactivation in accommodating multistage deformation in the Southwestern margin of the Ulleung Basin, East Sea (Sea of Japan): Insights from 3D seismic interpretation. Mar. Petrol. Geol. 158, 106511. https://doi.org/10.1016/j.marpetgeo.2023.106511.
Kim, Y.S., Sanderson, D.J., 2005. The relationship between displacement and length of faults: A review. Earth Sci. Rev. 68 (3–4), 317–334. https://doi.org/10.1016/j.earscirev.2004.06.003.
Klinkmüller, M., Schreurs, G., Rosenau, M., et al., 2016. Properties of granular analogue model materials: A community wide survey. Tectonophysics 684, 23–38. https://doi.org/10.1016/j.tecto.2016.01.017.
Li, C.F., Xu, X., Lin, J., et al., 2014. Ages and magnetic structures of the South China Sea constrained by deep tow magnetic surveys and IODP Expedition 349. G-cubed 15 (12), 4958–4983. https://doi.org/10.1002/2014GC005567.
Li, G., Mei, L.F., Ye, Q., et al., 2023. Post-rift faulting controlled by different geodynamics in the Pearl River Mouth Basin, northern South China Sea margin. Earth Sci. Rev. 237, 104311. https://doi.org/10.1016/j.earscirev.2022.104311.
Li, S.Z., Suo, Y.H., Li, X.Y., et al., 2019. Mesozoic tectono-magmatic response in the East Asian ocean–continent connection zone to subduction of the Paleo-Pacific Plate. Earth Sci. Rev. 192, 91–137. https://doi.org/10.1016/j.earscirev.2019.03.003.
Li, W., Cao, M.Y., Wang, D., et al., 2024. Cenozoic structure of the Zhu 3 Depression in the Pearl River Mouth Basin and its response to the dynamic background of the South China Sea. J. Geol. Soc. 181 (4), jgs2023-j2119. https://doi.org/10.1144/jgs2023-119.
Li, Z.X., Li, X.H., 2007. Formation of the 1300-km-wide intracontinental orogen and postorogenic magmatic province in Mesozoic South China: A flat-slab subduction model. Geology 35 (2), 179–182. https://doi.org/10.1130/G23193A.1.
Liu, Y.M., Wu, Z.P., Liu, L.J., et al., 2021. Cenozoic structure and tectonics of north subbasins in Beibu Gulf basin, northern south China Sea. Tectonophysics 812, 228912. https://doi.org/10.1016/j.tecto.2021.228912.
Lohrmann, J., Kukowski, N., Adam, J., et al., 2003. The impact of analogue material properties on the geometry, kinematics, and dynamics of convergent sand wedges. J. Struct. Geol. 25 (10), 1691–1711. https://doi.org/10.1016/S0191-8141(03)00005-1.
Lou, R., Sun, Y.H., Fan, T.G., et al., 2022. Influence of multi-trend major fault reactivation during multiphase rifting: Beier Depression, Hailar Basin, NE China. Geol. Mag. 159 (10), 1767–1786. https://doi.org/10.1017/S0016756822000565.
Ma, Q., Qian, S.P., Xu, Y.G., et al., 2025. Architecture and evolution of the lithosphere beneath the northern South China Sea: Implications for plate-edge lithospheric thinning and rifting. Fundam. Res. https://doi.org/10.1016/j.fmre.2025.03.002.
Ma, X.Q., Liu, J., Zhu, D.W., et al., 2021. Sedimentary response of multiphase strike-slip pull-apart basins: A case study from the Pearl River Mouth Basin, northern South China Sea. Geotect. Metallogenia 45 (1), 64–78. https://doi.org/10.16539/j.ddgzyckx.2021.01.006 (in Chinese).
Maunde, A., Alves, T.M., 2022. Effect of tectonic inversion on supra-salt fault geometry and reactivation histories in the Southern North Sea. Mar. Petrol. Geol. 135, 105401. https://doi.org/10.1016/j.marpetgeo.2021.105401.
Maunde, A., Alves, T.M., Moore, G.F., 2021. Shallow fault systems of thrust anticlines responding to changes in accretionary prism lithology (Nankai, SE Japan). Tectonophysics 812, 228888. https://doi.org/10.1016/j.tecto.2021.228888.
Moeck, I., Kwiatek, G., Zimmermann, G., 2009. Slip tendency analysis, fault reactivation potential and induced seismicity in a deep geothermal reservoir. J. Struct. Geol. 31 (10), 1174–1182. https://doi.org/10.1016/j.jsg.2009.06.012.
Morley, C.K., 2002. A tectonic model for the Tertiary evolution of strike-slip faults and rift basins in SE Asia. Tectonophysics 347 (4), 189–215. https://doi.org/10.1016/S0040-1951(02)00061-6.
Morley, C.K., 2012. Late cretaceous–early Palaeogene tectonic development of SE Asia. Earth Sci. Rev. 115 (1–2), 37–75. https://doi.org/10.1016/j.earscirev.2012.08.002.
Morley, C.K., 2016. Major unconformities/termination of extension events and associated surfaces in the South China Seas: Review and implications for tectonic development. J. Asian Earth Sci. 120, 62–86. https://doi.org/10.1016/j.jseaes.2016.01.013.
Natale, J., Vitale, S., Isaia, R., 2024. Simultaneous normal and reverse faulting in reactivating caldera faults: A detailed field structural analysis from Campi

Flegrei (southern Italy). J. Struct. Geol. 181, 105109. https://doi.org/10.1016/j.jsg.2024.105109.
Peacock, D.C.P., 2002. Propagation, interaction and linkage in normal fault systems. Earth Sci. Rev. 58 (1–2), 121–142. https://doi.org/10.1016/S0012-8252(01)00085-X.
Peacock, D.C.P., Sanderson, D.J., 1991. Displacements, segment linkage and relay ramps in normal fault zones. J. Struct. Geol. 13 (6), 721–733. https://doi.org/10.1016/0191-8141(91)90033-F.
Peng, X., Li, C.F., 2024. Along-strike break-up variations of the continent–ocean transition zone in the northern South China Sea. J. Geol. Soc. 181 (2) jgs2023-j2134. https://doi.org/10.1144/jgs2023-134.
Peng, X., Li, C.F., Shen, C.B., et al., 2022. Intra-basement structures and their implications for rifting of the northeastern South China Sea margin. J. Asian Earth Sci. 225, 105073. https://doi.org/10.1016/j.jseaes.2021.105073.
Phillips, T.B., Fazlikhani, H., Gawthorpe, R.L., et al., 2019. The influence of structural inheritance and multiphase extension on rift development in the northern North Sea. Tectonics 38 (12), 4099–4126. https://doi.org/10.1029/2019TC005756.
Phillips, T.B., McCaffrey, K.J.W., 2019. Terrane boundary reactivation, barriers to lateral fault propagation and reactivated fabrics: rifting across the median batholith zone, great South Basin, New Zealand. Tectonics 38 (11), 4027–4053. https://doi.org/10.1029/2019TC005772.
Pichot, T., Delescluse, M., Chamot-Rooke, N., et al., 2014. Deep crustal structure of the conjugate margins of the SW South China Sea from wide-angle refraction seismic data. Mar. Petrol. Geol. 58, 627–643. https://doi.org/10.1016/j.marpetgeo.2013.10.008.
Ryan, L., Magee, C., Jackson, C.A.L., 2017. The kinematics of normal faults in the Ceduna Subbasin, offshore southern Australia: Implications for hydrocarbon trapping in a frontier basin. AAPG Bull. 101 (3), 321–341. https://doi.org/10.1306/08051615234.
Samsu, A., Micklethwaite, S., Williams, J.N., et al., 2023. Structural inheritance in amagmatic rift basins: manifestations and mechanisms for how pre-existing structures influence rift-related faults. Earth Sci. Rev. 246, 104568. https://doi.org/10.1016/j.earscirev.2023.104568.
Savva, D., Pubellier, M., Franke, D., et al., 2014. Different expressions of rifting on the South China Sea margins. Mar. Petrol. Geol. 58, 579–598. https://doi.org/10.1016/j.marpetgeo.2014.05.023.
Schiffer, C., Doré, A.G., Foulger, G.R., et al., 2020. Structural inheritance in the North Atlantic. Earth Sci. Rev. 206, 102975. https://doi.org/10.1016/j.earscirev.2019.102975.
Serck, C.S., Braathen, A., 2019. Extensional fault and fold growth: Impact on accommodation evolution and sedimentary infill. Basin Res. 31 (5), 967–990. https://doi.org/10.1111/bre.12353.
Shi, H.S., Du, J.Y., Mei, L.F., et al., 2020. Huizhou Movement and its significance in Pearl River Mouth Basin, China. Petrol. Explor. Dev. 47 (3), 447–461. https://doi.org/10.11698/PED.2020.03.02 (in Chinese).
Shi, H.S., Li, C.F., 2012. Mesozoic and early Cenozoic tectonic convergence-to-rifting transition prior to opening of the South China Sea. Int. Geol. Rev. 54 (15), 1801–1828. https://doi.org/10.1080/00206814.2012.677136.
Shi, Y.L., Long, Z.L., Zhang, X.T., et al., 2023. Exploring the dynamic hydrocarbon accumulation process of the Enping 17 sub-sag in the Enping Sag, Pearl River Mouth Basin. Oil Gas Geol. 44 (5), 1279–1289 (in Chinese). https://doi.org/10.11743/ogg20230516
Shi, H.S., Yu, S.M., Mei, L.F., et al., 2009. Features of Paleogene episodic rifting in Huizhou fault depression in the Pearl River Mouth Basin. Nat. Gas. Ind. 29 (1), 35–37+40+133 (in Chinese).
Shu, L.S., Faure, M., Wang, B., et al., 2008. Late Palaeozoic–Early Mesozoic geological features of South China: Response to the Indosinian collision events in Southeast Asia. C. R. Geosci. 340 (2–3), 151–165. https://doi.org/10.1016/j.crte.2007.10.010.
Strugale, M., da Silva Schmitt, R., Cartwright, J., 2021. Basement geology and its controls on the nucleation and growth of rift faults in the northern Campos Basin, offshore Brazil. Basin Res. 33 (3), 1906–1933. https://doi.org/10.1111/bre.12540.
Taghipour, M., Ghafoori, M., Lashkaripour, G.R., et al., 2019. Estimation of the current stress field and fault reactivation analysis in the Asmari reservoir, SW Iran. Pet. Sci. 16, 513–526. https://doi.org/10.1007/s12182-019-0331-9.
Tang, X., Yu, Y.X., Zhang, X.T., et al., 2023. Multiphase faults activation in the southwest Huizhou Sag, Pearl River Mouth Basin: Insights from 3D seismic data. Mar. Petrol. Geol. 152, 106257. https://doi.org/10.1016/j.marpetgeo.2023.106257.
Thorsen, C.E., 1963. Age of growth faulting in southeast Louisiana. Gulf Coast Assoc. Geol. Soc. Trans. 13, 103–110.
Tong, H.M., 2012. Sandbox modeling of fault formation and evolution in the Weixinan Sag, Beibuwan Basin, China. Pet. Sci. 9, 121–128. https://doi.org/10.1007/s12182-012-0192-y.
Tong, H.M., Koyi, H., Huang, S., et al., 2014. The effect of multiple pre-existing weaknesses on formation and evolution of faults in extended sandbox models. Tectonophysics 626, 197–212. https://doi.org/10.1016/j.tecto.2014.04.046.
Tong, H.M., Yin, A., 2011. Reactivation tendency analysis: A theory for predicting the temporal evolution of preexisting weakness under uniform stress state. Tectonophysics 503 (3–4), 195–200. https://doi.org/10.1016/j.tecto.2011.02.012.
Tron, V., Brun, J.P., 1991. Experiments on oblique rifting in brittle-ductile systems. Tectonophysics 188 (1–2), 71–84. https://doi.org/10.1016/0040-1951(91)90315-J.
Tvedt, A.B.M., Rotevatn, A., Jackson, C.A.L., et al., 2013. Growth of normal faults in multilayer sequences: A 3D seismic case study from the Egersund Basin, Norwegian North Sea. J. Struct. Geol. 55, 1–20. https://doi.org/10.1016/j.jsg.2013.08.002.
Underhill, J.R., Richardson, N., 2022. Geological controls on petroleum plays and future opportunities in the North Sea Rift Super Basin. AAPG Bull. 106 (3), 573–631. https://doi.org/10.1306/07132120084.
Van den Bogert, P.A.J., Van Eijs, R.M.H.E., 2020. Why Mohr-circle analyses may underestimate the risk of fault reactivation in depleting reservoirs. Int. J. Rock Mech. Min. Sci. 136, 104502. https://doi.org/10.1016/j.ijrmms.2020.104502.
Wang, D., Yang, L.L., Li, W., et al., 2023. The impact of pre-existing faults on fault geometry during multiphase rifts: the Jiyang Depression, Eastern China. J. Mar. Sci. Eng. 11 (10), 1971. https://doi.org/10.3390/jmse11101971.
Wang, D., Zhang, X.Q., Yang, L.L., et al., 2022. Influence of pre-existing faults on Cenozoic structures in the Chengbei sag and the Wuhaozhuang area, Bohai Bay Basin, East China. Mar. Petrol. Geol. 138, 105539. https://doi.org/10.1016/j.marpetgeo.2022.105539.
Wang, P.C., Li, S.Z., Suo, Y.H., et al., 2021. Structural and kinematic analysis of Cenozoic rift basins in South China Sea: A synthesis. Earth Sci. Rev. 216, 103522. https://doi.org/10.1016/j.earscirev.2021.103522.
Wang, W., Ye, J.R., Yang, X.H., et al., 2015. Sediment provenance response to Paleogene multi-phase rift cycles in the Huizhou Sag, Pearl River Mouth Basin. Earth Sci. (J. China Univ. Geosci.). 40 (6), 1061–1071 (in Chinese).
Webber, S., Little, T., Boulton, C., et al., 2022. Regional-scale low-angle normal fault friction and cohesion constrained from Mohr-Coulomb models of active and abandoned range-front faults in Papua New Guinea. J. Geophys. Res. Solid Earth 127 (4), e2021JB023553. https://doi.org/10.1029/2021JB023553.
Weijermars, R., 1986. Flow behaviour and physical chemistry of bouncing putties and related polymers in view of tectonic laboratory applications. Tectonophysics 124 (3–4), 325–358. https://doi.org/10.1016/0040-1951(86)90208-8.
Whipp, P.S., Jackson, C.A.L., Gawthorpe, R.L., et al., 2014. Normal fault array evolution above a reactivated rift fabric; a subsurface example from the northern Horda Platform, Norwegian North Sea. Basin Res. 26 (4), 523–549. https://doi.org/10.1111/bre.12050.
Withjack, M.O., Henza, A.A., Schlische, R.W., 2017. Three-dimensional fault geometries and interactions within experimental models of multiphase extension. AAPG Bull. 101 (11), 1767–1789. https://doi.org/10.1306/02071716090.
Withjack, M.O., Jamison, W.R., 1986. Deformation produced by oblique rifting. Tectonophysics 126 (2–4), 99–124. https://doi.org/10.1016/0040-1951(86)90255-2.
Wu, Z., Zhu, W.L., Shao, L., et al., 2016. Sedimentary facies and the rifting process during the late Cretaceous to early Oligocene in the northern continental margin, South China Sea. Interpretation 4 (3), SP33–SP45. https://doi.org/10.1190/INT-2015-0163.1.
Xiong, W.L., Zhu, J.Z., Yang, X.Y., et al., 2020. Study on hydrocarbon sources and accumulation process in the northern uplift structural belt of the Enping Sag. China Offshore Oil Gas 32 (1), 54–65 (in Chinese). https://doi.org/CNKI:SUN:ZHSD.0.2020-01-006.
Ye, Q., Mei, L.F., Shi, H.S., et al., 2018a. A low-angle normal fault and basement structures within the Enping Sag, Pearl River Mouth Basin: Insights into late Mesozoic to early Cenozoic tectonic evolution of the South China Sea area. Tectonophysics 731–732, 1–16. https://doi.org/10.1016/j.tecto.2018.03.003.
Ye, Q., Mei, L.F., Shi, H.S., et al., 2018b. The Late Cretaceous tectonic evolution of the South China Sea area: An overview, and new perspectives from 3D seismic reflection data. Earth Sci. Rev. 187, 186–204. https://doi.org/10.1016/j.earscirev.2018.09.013.
Ye, Q., Mei, L.F., Shi, H.S., et al., 2020. The influence of pre-existing basement faults on the Cenozoic structure and evolution of the proximal domain, northern South China Sea rifted margin. Tectonics 39 (3), e2019TC005845. https://doi.org/10.1029/2019TC005845.
Yin, A., 2010. Cenozoic tectonic evolution of Asia: A preliminary synthesis. Tectonophysics 488 (1–4), 293–325. https://doi.org/10.1016/j.tecto.2009.06.002.
Žalohar, J., Vrabec, M., 2010. Kinematics and dynamics of fault reactivation: the Cosserat approach. J. Struct. Geol. 32 (1), 15–27. https://doi.org/10.1016/j.jsg.2009.06.008.
Zhang, Y.Z., Qi, J.F., Wu, J.F., 2019. Cenozoic fault systems and tectono-dynamic controls of northern South China Sea basins. Earth Sci. 44 (2), 603–625 (in Chinese). https://doi.org/10.3799/dqkx.2018.542
Zhao, F., Alves, T.M., Xia, S.H., et al., 2020. Along-strike segmentation of the South China Sea margin imposed by inherited pre-rift basement structures. Earth Planet Sci. Lett. 530, 115862. https://doi.org/10.1016/j.epsl.2019.115862.
Zhu, D.W., Peng, G.R., Zhang, Z.T., et al., 2022. Hydrocarbon accumulation conditions in the northern drape belt of the Enping Sag, Pearl River Mouth Basin. China Offshore Oil Gas 34 (1), 36–44 (in Chinese). https://doi.org/10.11935/j.issn.1673-1506.2022.01.005
Zhu, W.L., Wu, J.F., Zhang, G.C., et al., 2015. Discrepancy tectonic evolution and petroleum exploration in China offshore Cenozoic basins. Earth Sci. Front. 22 (1), 88–101. https://doi.org/10.13745/j.esf.2015.01.008 (in Chinese).
Zoback, M.D., Townend, J., 2001. Implications of hydrostatic pore pressures and high crustal strength for the deformation of intraplate lithosphere. Tectonophysics 336 (1–4), 19–30. https://doi.org/10.1016/S0040-1951(01)00091-9.
Zou, Y.Y., Maestrelli, D., Corti, G., et al., 2024. Influence of inherited brittle fabrics on continental rifting: Insights from centrifuge experimental modeling and application to the East African Rift System. Tectonics 43 (1), e2023TC007947. https://doi.org/10.1029/2023TC007947.
Zwaan, F., Schreurs, G., 2017. How oblique extension and structural inheritance influence rift segment interaction: insights from 4D analog models. Interpretation 5 (1), SD119–SD138. https://doi.org/10.1190/INT-2016-0063.1.